Piezoresistive MXene/Silk fibroin nanocomposite hydrogel for accelerating bone regeneration by Re-establishing electrical microenvironment

Zhi-Chao Hu [a,1], Jia-Qi Lu [a,1], Tai-Wei Zhang [a,1], Hai-Feng Liang [a,1], Hao Yuan [b], Di-Han Su [a], Wang Ding [c], Rui-Xian Lian [d], Yu-Xiang Ge [c], Bing Liang [e], Jian Dong [a,***], Xiao-Gang Zhou [a,**], Li-Bo Jiang [a,*]

[a] *Department of Orthopaedic Surgery, Zhongshan Hospital, Fudan University, Shanghai, 200032, China*
[b] *Key Laboratory of Advanced Display and System Applications of Ministry of Education, Shanghai University, Shanghai, 200072, China*
[c] *Department of Orthopedics Surgery, Minhang Hospital, Fudan University, Shanghai, 201100, China*
[d] *Key Laboratory for Ultrafine Materials of Ministry of Education, Frontiers Science Center for Materiobiology and Dynamic Chemistry, Research Center for Biomedical Materials of Ministry of Education, School of Materials Science and Engineering, East China University of Science and Technology, Shanghai, 200237, China*
[e] *Department of Orthopedic Surgery, Zhongshan Hospital (Xiamen), Fudan University, Xiamen, 361015, China*

ARTICLE INFO

ABSTRACT

The electrical microenvironment plays an important role in bone repair. However, the underlying mechanism by which electrical stimulation (ES) promotes bone regeneration remains unclear, limiting the design of bone microenvironment–specific electroactive materials. Herein, by simple co-incubation in aqueous suspensions at physiological temperatures, biocompatible regenerated silk fibroin (RSF) is found to assemble into nanofibrils with a β-sheet structure on MXene nanosheets, which has been reported to inhibit the restacking and oxidation of MXene. An electroactive hydrogel based on RSF and bioencapsulated MXene is thus prepared to promote efficient bone regeneration. This MXene/RSF hydrogel also acts as a piezoresistive pressure transducer, which can potentially be utilized to monitor the electrophysiological microenvironment. RNA sequencing is performed to explore the underlying mechanisms, which can activate Ca^{2+}/CALM signaling in favor of the direct osteogenesis process. ES is found to facilitate indirect osteogenesis by promoting the polarization of M2 macrophages, as well as stimulating the neogenesis and migration of endotheliocytes. Consistent improvements in bone regeneration and angiogenesis are observed with MXene/RSF hydrogels under ES *in vivo*. Collectively, the MXene/RSF hydrogel provides a distinctive and promising strategy for promoting direct osteogenesis, regulating immune microenvironment and neovascularization under ES, leading to re-establish electrical microenvironment for bone regeneration.

1. Introduction

Electrical energy is a component of the human body [1], and the electrical microenvironment is considered crucial for numerous physiological activities such as tissue regeneration, muscle contraction and embryogenesis [2]. Due to the biological electrical characteristics of the bone microenvironment, exogenous electrical stimulation (ES), which manipulates transmembrane potentials, could potentially be utilized to regulate the osteogenic function of osteoblasts or osteoblast-like cells [3]. Although external ES may cause side effect such as the risk of infection, it has been successfully used in the field of orthopedics owing to its excellent therapeutic potential for the refractory and non-union fractures; recently, it has also attracted a large amount of interest as an adjunct therapy in the engineering of bone tissue regeneration [4–6]. However, owing to the complexity of the bone microenvironment, the underlying mechanism by which ES promotes bone regeneration

remains unknown, which leads to difficulties when designing bone-specific electroactive materials.

Hydrogels are flexible scaffolds that have various biological properties [7–9]. However, owing to a lack of electron or ion flow, three-dimensional (3D) networks of pure hydrogels typically consist of several chemical and physical interactions that have poor electrical conductivity [10,11]. It has been reported that two-dimensional (2D) materials can be adopted into polymer networks to effectively change the properties of newly formed hydrogels [12]. MXenes, as novel 2D nanomaterials composed of transition metal complexes, have previously been utilized in biomedicine owing to their metallic conductivity, piezoelectric effect, excellent hydrophilicity, and rich variety of surface chemical properties [13,14]. Although there are many other electroactive materials, such as polyvinylidene fluoride (PVDF), graphene, carbon nanotubes, and black phosphorus, their applications are limited. For example, owing to the poor water solubility of PVDF, graphene, and carbon nanotubes, they do not bind with other materials easily [15,16], while the black phosphorus degrades easily owing to the inherent instability [17]. In contrast, the numerous adjustable functional groups on the surface of MXene reduced its oxidation upon storage and use as well as endowed it with high water dispersion and plasticity to form various composites and micro-structures by combining with other

materials [15,18]. However, without proper surface modification, the tendency to oxidize in wet environments and restack in aqueous solutions over time may still result in an obvious reduction in conductivity [19]. Numerous studies have combined these prepared 2D nanomaterials with biopolymers to synthetize new nanocomposites with better mechanical performance, retained electrical conductivity, stability, or additive properties [20–22]. Specifically, biopolymers acquired from natural ingredients, such as amino acids, proteins, and polysaccharides, have been adopted to develop into a variety of nanohybrids based on their interactions with synthetic 2D nanomaterials [23]. However, limited studies have been reported on MXene-biopolymer nanohybrids or related materials for bone regeneration [24]. Michelle et al. reported that the polymer coating of MXene could hinder its surface oxidation and extend its storage life [25]. Lin et al. found that an electroactive MXene hydrogel could accelerate the healing process of skin wound by coupling ES [26]. Ye et al. reported that the preparation of conductive Ti_2C-cryogels promoted the functional maturation of cardiomyocytes and the repair of myocardial infarction [27]. Regenerated silk fibroin (RSF), as a protein with excellent mechanical properties, good biocompatibility, and tunable biodegradability extracted from Bombyx mori worms, is one of the most widely explored biopolymer materials for these purposes [28]. Notably,
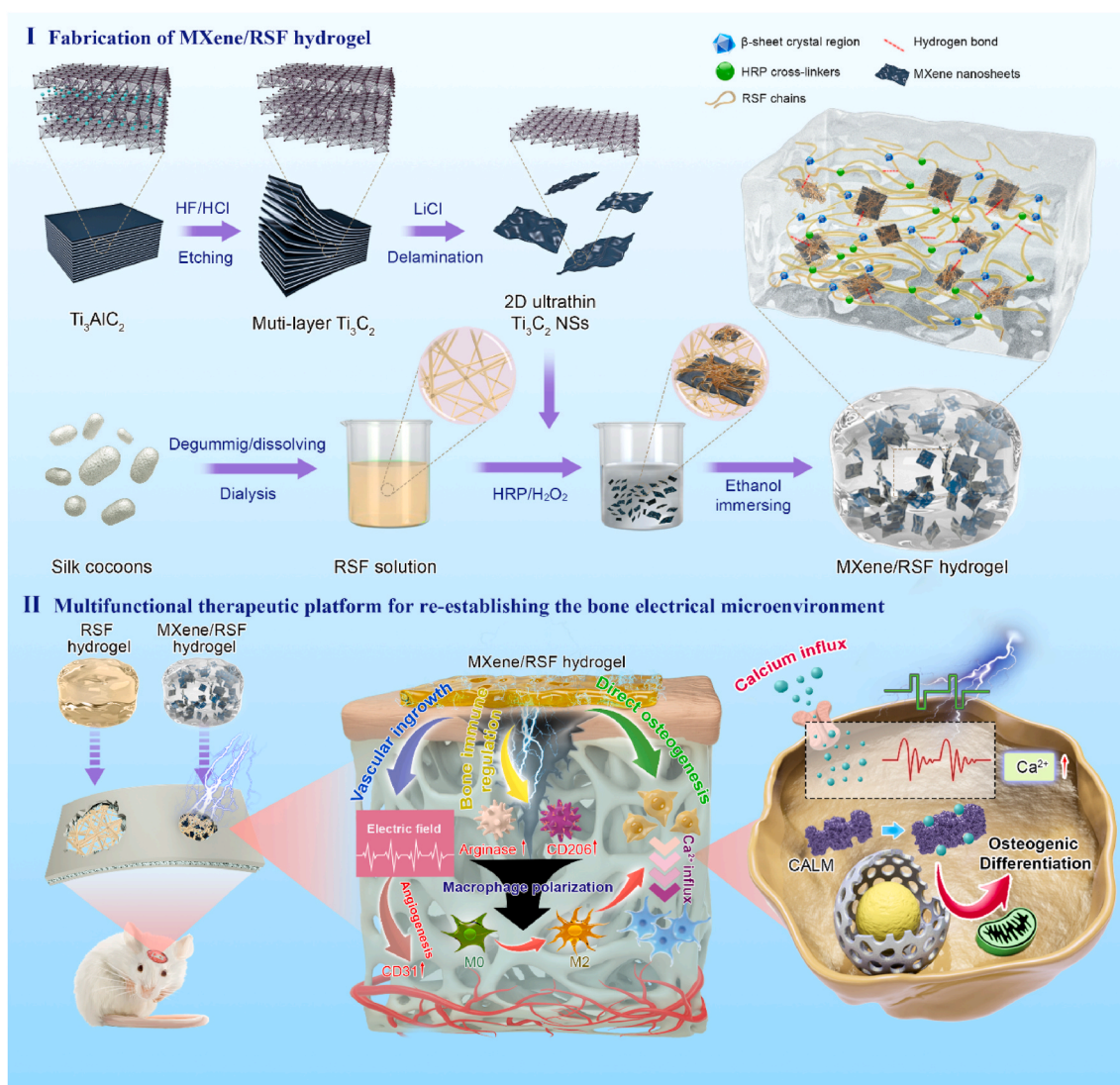
Scheme 1. Schematic showing the fabrication and application of multifunctional electroactive hydrogels for the diversified treatment of bone defects. (I) Fabrication process for an MXene/RSF hydrogel. (II) Conceptual and effective mechanisms of the electroactive MXene/RSF hydrogels to re-establish the electrical microenvironment for bone regeneration.

its promising features, such as processability and abundant surface functional groups, allow for interactions with 2D nanomaterials, which contributed to the ideal design of fibroin with the overall hierarchy [29]. Ling et al. reported a novel hybrid nanocomposite via a facile one-step protocol, where silk nanofibrils directly grew on graphene surfaces [22]. This co-assembled formulation will lead to an improved performance to enhance the stability of 2D materials in a variety of applications [22,25,29,30].

In this study, we developed RSF-bioencapsulated MXene nanosheets using a co-assemblage and subsequently incorporated the modified MXene into the RSF solution to form an MXene/RSF dual-crosslinked network nanocomposite hydrogel using horseradish peroxidase (HRP) and hydrogen peroxide (H_2O_2) (Scheme 1). Then, we evaluated cytocompatibility, electrical conductivity, osteoinductivity, bone immunoregulatory capacity, and angiogenesis ability *in vitro*. The mechanism by which electrical stimulation promotes osteogenic differentiation has also been explored. In addition, its therapeutic potential in bone regeneration and neovascularization *in vivo* was investigated using a critical-size calvarial bone defect model. We hope this multifunctional conductive hydrogel can provide a distinctive biosystem to enrich the potential of the application in bone regeneration.

2. Results and discussion

2.1. Characterization of MXene-RSF interactions

Interactions between 2D materials and polymers are the basis for synthesizing co-assembled nanocomposites with enhanced stability [25, 29]. Currently, the characterization of morphology and structure were explored to determine the interactions between RSF and MXene. The relevant characterization of the RSF and MXene/RSF solution is shown in Fig. 1. Transmission electron microscopy (TEM), scanning electron microscopy (SEM) and Cryo-SEM were performed to detect morphological changes, including those for the pure RSF and MXene/RSF solutions in a 37 °C water bath after 72 h (Fig. 1A–C). TEM images (Fig. 1A) indicated the gradual reorganization of non-specific morphology into unordered long nanofibrils over the course of 72 h in the pure RSF diluted solution. When the RSF was co-incubated with MXene nanosheets, instead of a single layer of MXene, the nanosheet was covered by densely packed nanofibrils, especially on its edge. This indicated that most of the RSF molecules could be selectively adsorbed and regenerated to nanofibrils on the MXene nanosheets. SEM (Fig. 1B) showed the morphology of the solutions after freeze-drying, where more apparent hierarchical nanofibril structures were observed in the MXene/RSF group after co-culturing for 72 h, and the pure RSF in comparison showed a denser unordered appearance with RSF fibrils, confirming
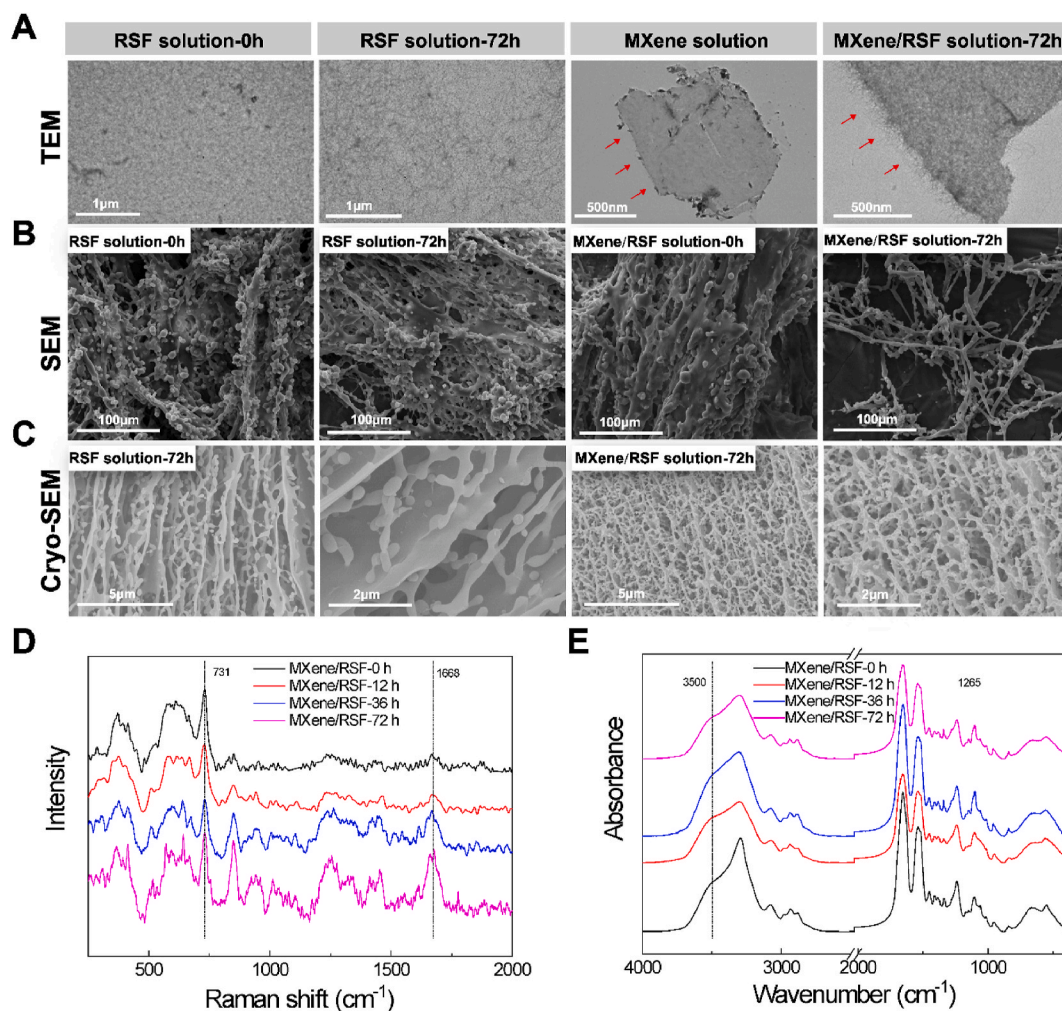
Fig. 1. Characterization of the MXene-RSF interactions in solution. (A, B) TEM and SEM images of the pure RSF and MXene/RSF hybrid after assembly for 0 and 72 h. Red arrows indicate the morphology of the edge of MXene nanosheet. (C) Cryo-SEM images of the pure RSF and MXene/RSF hybrid after assembly for 72 h. (D) Raman spectra of MXene/RSF solution after incubation at 37 °C for different durations. (E) FT-IR spectra of MXene/RSF solution after incubation at 37 °C for different durations.

in situ nanofibril growth with thermal incubation. Cryo-SEM (Fig. 1C) also showed the nanofibril morphology, which was more obvious in the MXene-containing solution than in the pure RSF solution, indicating that MXene may accelerate the formation of RSF nanofibril structures. The directed assembly of the RSF nanofibrils on MXene in this study may be closely linked to the complex surface functional groups of MXene [31]. Time-related Raman shift spectra and Fourier transform infrared spectra (FT-IR) were obtained to investigate the interactions between Ti$_3$C$_2$ MXene and RSF after being co-cultured for up to 72 h (Fig. 1D, E). A mixed solution was prepared for further testing by quenching in liquid nitrogen. The existence of β-sheets in RSF was confirmed by the Raman spectra at approximately 1668 cm^{-1}, which has been described as the fingerprint of the β-sheet [32,33]. Characteristic peaks at 731 cm^{-1} in the Raman spectra were observed for Ti$_3$C$_2$ MXene, which were consistent with the reported data [34]. Most importantly, the intensity of the peaks for the β-sheet increased with time in the MXene/RSF samples, indicating that Ti$_3$C$_2$ MXene might promote RSF nanofibril assembly by enhancing the formation of the β-sheet structure. This could be attributed to the fact that the stability of hydrophobic β-sheets has been enhanced after the contact of RSF chains with a heterogeneous hydrophilic surface of MXene [35–37]. FT-IR results showed a secondary structure change during the incubation time. For the MXene/RSF solution, the distinctive absorption peaks of the β-sheet near 1265 cm^{-1} showed increasing intensity with the co-assembly incubation time, indicating that the increase in β-sheet structure corresponds to the nanofibril morphology observed in the TEM and SEM tests and is consistent with the conclusions made from the morphological observations [38]. In addition, the stretching vibration peak of MXene at 3500 cm^{-1} corresponds to O–H stretching [39,40]. After adding MXene nanosheets, the infrared vibration peak shifted to the left, which is associated with the interaction between RSF and MXene. To sum up, these groups and interactions might be the reason for the promotion of nanofibril formation on MXene surface. According to a previous study [25], this dense as well as hydrophobic β-sheets structure induced the protective shell of the RSF nanofibril, which could alleviate surface oxidation and enhance disperison stability of the MXenes. Additionally, we conducted ultraviolet–visible (UV–vis) spectroscopy to investigate the oxidation of MXenes (Fig. S1). The changes in UV–vis spectra were similar to Michelle's study, which indicated that RSF encapsulation could partly inhibit the oxidation of MXene [25].
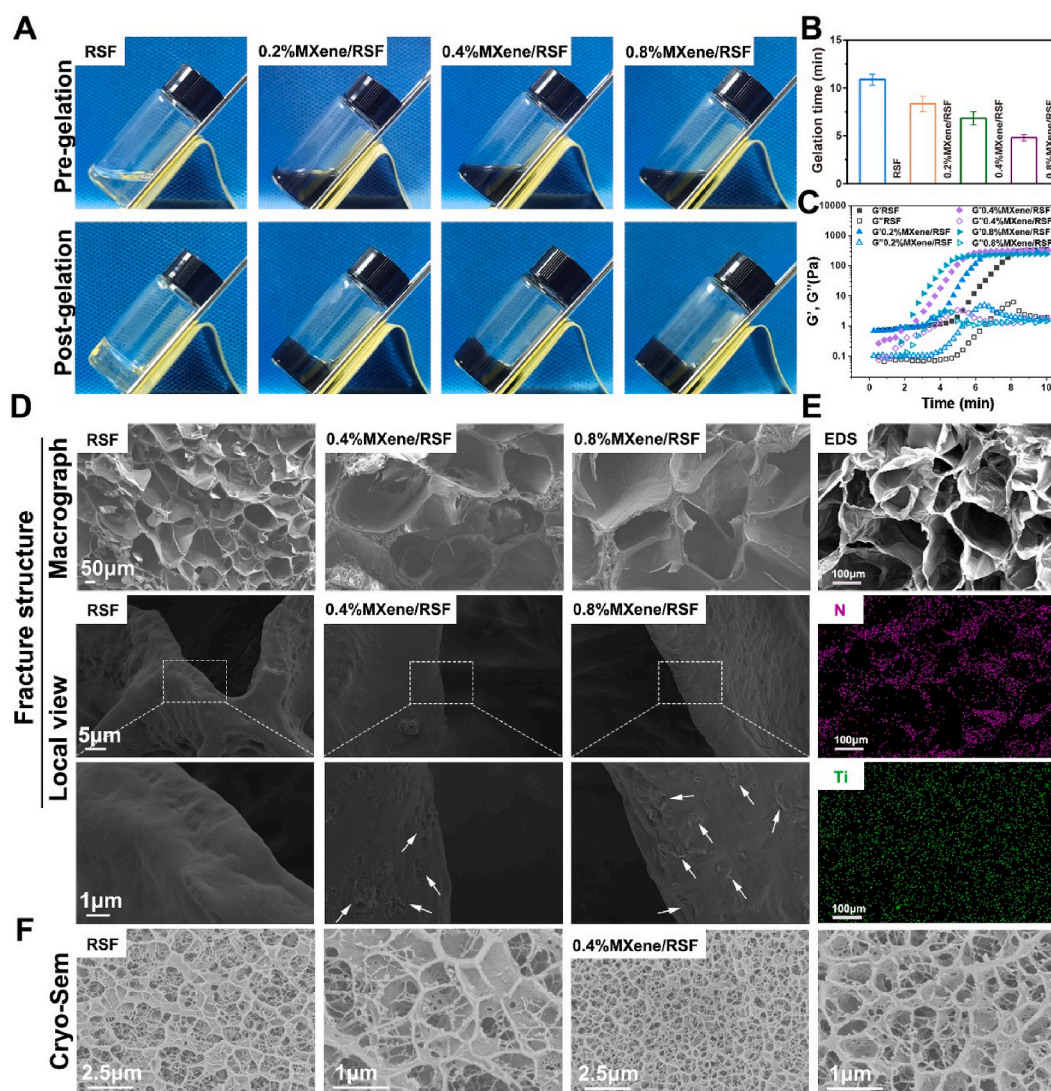
Fig. 2. Gelation behavior and morphology characterization of the MXene/RSF hydrogels. (A) Digital photos of MXene/RSF solutions (up) and MXene/RSF hydrogels (down). (B) Gelation times for the different hydrogel samples with increasing concentrations of MXene. (C) Rheological properties exhibiting the G′ and G″ of various hydrogels. (D) SEM images showing the fracture morphology of hydrogel samples. (E) Fracture structure and element mapping of the MXene/RSF hydrogel. (F) Cryo-SEM images of the RSF and 0.4%MXene/RSF hydrogels.

2.2. Physicochemical structure and multifunctional properties of MXene/RSF hydrogels

MXene/RSF dual crosslinked hydrogels were crosslinked by HRP and H$_2$O$_2$, followed by immersion in the 75% ethanol solution to form the uniform beta sheet structure with the secondary physical crosslinking. Interestingly, we found that the gelation time decreased significantly with the addition of MXene, indicating that it could accelerate the gelation process for the RSF hydrogel (Fig. 2A, **B**), which may be ascribed to the rich hydroxyl groups existing on MXene, providing more

hydrogen bonding sites for RSF and MXene [23,41]. Rheology analyses using time sweep tests were also conducted (Fig. 2C), where both the values of the storage (G′) and loss modulus (G″) increased abruptly in the RSF and MXene/RSF samples with thermal induction on the thermal platen, demonstrating the process of sol-gel transition. As the concentration of MXene increased, G′ and G″ grew faster and reached a plateau earlier, further suggesting that MXene could accelerate sol-gel transition. SEM and Cryo-SEM were carried out to observe the surface structure as well as internal/cross fracture morphology of the MXene/RSF hydrogels (Fig. 2D, **S2**, and **S3**). After introducing MXene nanosheets,
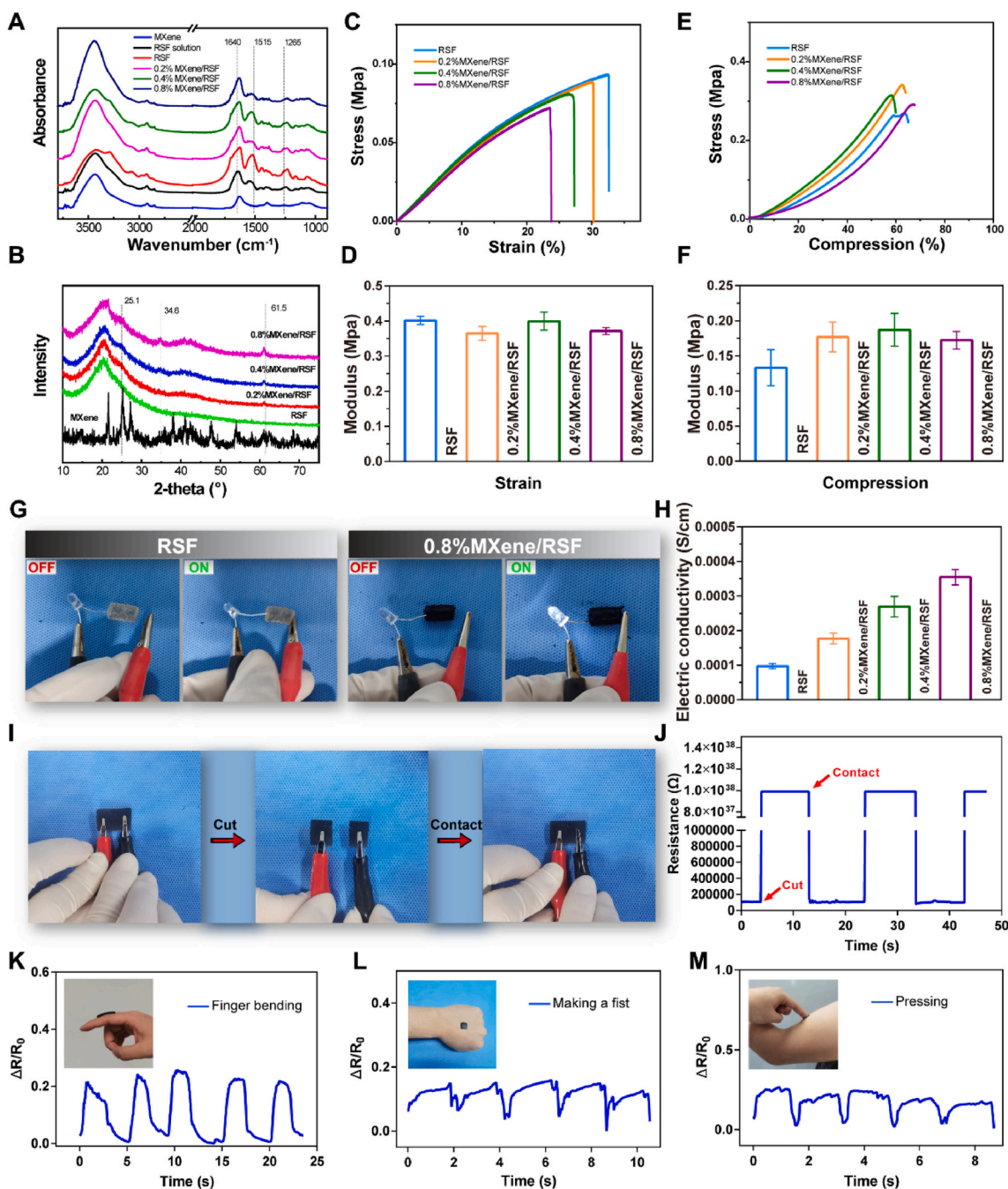
Fig. 3. Chemical structure and multifunctional properties of the MXene/RSF hydrogel. (A) FT-IR spectra of the RSF solution, MXene nanosheets, and RSF-based hydrogel samples. (B) XRD patterns of the different hydrogel samples. (C, D) Tensile stress–strain curves and elastic moduli for the different hydrogel samples. (E, F) Compressive stress–compression curves and compression moduli for the different hydrogel samples. (G) Electrically conductive pathways made of RSF and MXene/RSF hydrogels to illuminate an LED. (H) Electrical conductivity of hydrogels with various concentrations of MXene. (I, J) Cut-contact tests for the MXene/RSF hydrogel using a real-time resistance response. (K–M) Sensors assembled from MXene/RSF to monitor various human movements including finger bending, fisting, and pressing.

the surface morphology of the RSF-based hydrogels became increasingly rougher in a dose-dependent manner (Fig. S2), which might be beneficial for cell attachment and spreading. The fracture structure view suggested that the porous structures of the hydrogel system were not affected by the addition of MXene (Fig. 2D, and S3). As a control, relatively smooth morphology was found in the local SEM view of the RSF hydrogels without MXene integration, while the roughness of hydrogels increased as the content of MXenes increased, corresponding to the fact that an increasing number of MXenes were embedded in the MXene/RSF hydrogels. In addition, the scanning electron microscopy-energy dispersive spectroscopy (SEM-EDS) analyses of titanium was carried out in order to verify the homogeneous distribution of MXene in the RSF hydrogel (Fig. 2E, and S4). Cryo-SEM (Fig. 2F) further suggested that the porous structure of the RSF hydrogel was not affected by MXenes, and the nanofibril morphology of silk was observed, which was consistent with the reported silk fibroin hydrogel occurrence with an HRP enzyme crosslinker and ethanol-induced physical β-sheet crosslinkers [42].

The presence of β-sheets in the FT-IR spectra was confirmed near 1265 cm^{-1}, 1515 cm^{-1}, and 1640 cm^{-1} [38]. The characteristic peaks (especially at 1640 cm^{-1}) in the MXene/RSF hydrogel groups were enhanced compared with those in the RSF hydrogel group, indicating that the number of β-sheets in the RSF system might increase with the addition of MXene (Fig. 3A). With the increase of MXene content, the results of X-ray diffraction (XRD) showed a gradual enhancement of the characteristic MXene peaks in the MXene/RSF samples, suggesting a successful MXene incorporation (Fig. 3B). Fig. 3C–F showed the mechanical test results of the RSF-based hydrogels. Notably, the elongation at break decreased with an increase of MXene-sheet content, suggesting a decreased ductility. This phenomenon can be ascribed to the high concentration of MXene destroying the chemical (HRP crosslinks) or physical (hydrogen bonds) interactions between the RSF chains itself or between MXene and RSF chains, and rearranging the chains to a certain extent, which finally lead to a decrease in the elongation at break [26, 43]. However, no significant difference was found in the compressive modulus and elastic modulus, indicating that the addition of MXene did not affect the mechanical strength of the hydrogel. The electrical conductivity of hydrogels acts as an important carrier to stimulate cellular processes [44]. Herein, an obviously illuminated light-emitting diode (LED) were observed, particularly in a hydrogel-connected circuit with high concentrations of MXene (Fig. 3G). The electric conductivity of the hydrogels increased to approximately 4×10^{-4} S/cm when the MXene content reached 8 mg/mL (Fig. 3H), indicating the favorable electroactivity of the MXene/RSF hydrogels, and this was in accordance with the findings of a previous study [26]. Furthermore, we performed a cut-contact test to explore the conductivity of the MXene/RSF hydrogel (Fig. 3I, J). When the hydrogel circuit was cut off, the resistance of MXene/RSF rapidly rose to a stable open-circuit state. However, there was a full instantaneous recovery to its original value once the two separated hydrogels were recontacted again, demonstrating the uniform distribution of MXene within the RSF hydrogel. In addition, to monitor tiny motions, the potential of MXene/RSF hydrogel fabricating as a wearable sensor was also examined. The formula $\Delta R/R_0$ (%) = (R − R_0)/R_0 × 100% was applied to define the sensing response. The repeatable and regular electrical signals after different movements, including finger bending, fisting, and pressing are demonstrated in Fig. 3K-M, indicating that the sensor can detect tiny human motions. This will provide a basis for further detection of electrophysiology in the bone microenvironment in future studies. The degradation properties of hydrogels with or without ES are shown in Fig. S5. A time-dependent weight loss was observed in all the RSF-based hydrogels, while no statistical difference was found in the weight loss among the RSF, RSF + ES, 0.4%MXene/RSF and 0.4%MXene/RSF + ES groups, indicating that MXene and ES did not affect the process of degradation. We also performed inductively coupled plasma (ICP) tests for Ti element to explore the release of MXene in the degradation of RSF-based hydrogels, with

and without ES (Fig. S6). Similar results were detected, indicating that ES did not affect the release of MXene.

2.3. Effect of MXene/RSF hydrogels on BMSC proliferation and migration

Good biocompatibility is the prerequisite for the application of biomaterials in tissue repair [45]. Currently, CCK-8 assay was applied to evaluate cell viability. From day 0–7, the viability of the BMSCs in RSF-based hydrogels groups decreased as the concentration of MXene reached 8 mg/mL on days 3 and 7, indicating that MXene may be toxic to BMSCs at high concentrations (Fig. 4A). Thus, 4 mg/mL MXene was used in subsequent experiments. Besides, another evaluating indicator of biocompatibility is the hemolysis of blood cells [46]. According to previous studies, a hemolysis ratio (HR) which is less than 5% is considered available for biomaterials [47]. The HR ratios of the pure RSF, 0.2%MXene/RSF, 0.4%MXene/RSF, and 0.8%MXene/RSF hydrogels were 0.182%, 0.244%, 0.454%, and 0.611%, respectively, indicating no hemolysis and good blood compatibility (Fig. 4B). ES has been reported to influence cell behavior [48]. In the current study, a custom-designed device was adopted to further detect cell proliferation under ES (Fig. S7). Living/dead cell double staining was used to evaluate the cell proliferation on various hydrogel samples after ES (0–400 mV mm^{-1}) (Fig. 4C and S8). ES was found to induce a certain degree of cell proliferation even in the pure RSF group despite that this proliferation was significantly less than in the groups containing MXene. In the 0.2% MXene/RSF group, the number of green stained cells increased gradually when the ES potentials were limited within 200 mV mm^{-1}, and decreased at the potential of 400 mV mm^{-1}. However, in the 0.4% MXene/RSF group, the green stained cells increased within 100 mV mm^{-1} and began to decrease as the voltage got higher. Best effect on cell proliferation was detected in the 0.4%MXene/RSF hydrogel group with a stimulation voltage of 100 mV mm^{-1}. Moreover, we conducted CCK-8 assays to further evaluate the effect of 0.4%MXene/RSF hydrogel on cell proliferation, with gradual increase in voltage up to 100 mV mm^{-1}. As shown in Fig. S9, the cell viability increased with the increase in voltage, indicating that the effect of 0.4%MXene/RSF hydrogel on cell proliferation was the highest at 100 mV mm^{-1}. Thus, 100 mV mm^{-1} stimulation voltage and 0.4%MXene/RSF were chosen for the subsequent experiments. To further evaluate the effects of various interventions on BMSCs proliferation, Ki67 immunofluorescence staining was performed (Fig. 4D). Higher expression levels of Ki67 were observed in the 0.4% MXene/RSF + ES group than those in the control, RSF, and 0.4%MXene/RSF groups, whereas there were no significant differences between the control, RSF, and 0.4%MXene/RSF groups, indicating that the proliferation of BMSCs could be promoted by the external ES (Fig. S10). Next, the effects of the different hydrogel samples on cell migration *in vitro* were tested using a wound healing assay in a custom-designed device with hydrogel electrodes (Fig. 4E). Similarly, the scratch assay showed no obvious difference in migration between the control and RSF groups, while both 0.4%MXene/RSF and 0.4%MXene/RSF + ES groups significantly improved the covered areas, indicating that both MXene and external ES could induce the migration of BMSCs (Fig. 4F and S11).

2.4. Effect of MXene/RSF hydrogels on BMSCs osteogenic differentiation and macrophage polarization

Alkaline phosphatase (ALP) plays an important role in early osteogenic differentiation, whereas late-stage differentiation can be predicted using Alizarin Red S (ARS) staining [49]. Both ALP staining on day 7 and ARS staining on day 21 were carried out to demonstrate the osteogenic differentiation of BMSCs (Fig. 5A, B, and S12). The results illustrated that ALP and ARS staining were both enhanced by 0.4%MXene/RSF and 0.4%MXene/RSF + ES groups, indicating that both the presence of MXene and external ES promoted osteogenic differentiation. Immunofluorescence staining (RUNX-2 and Col-1) was performed to localize the osteogenic marker expression position and its amount in BMSCs on day 7
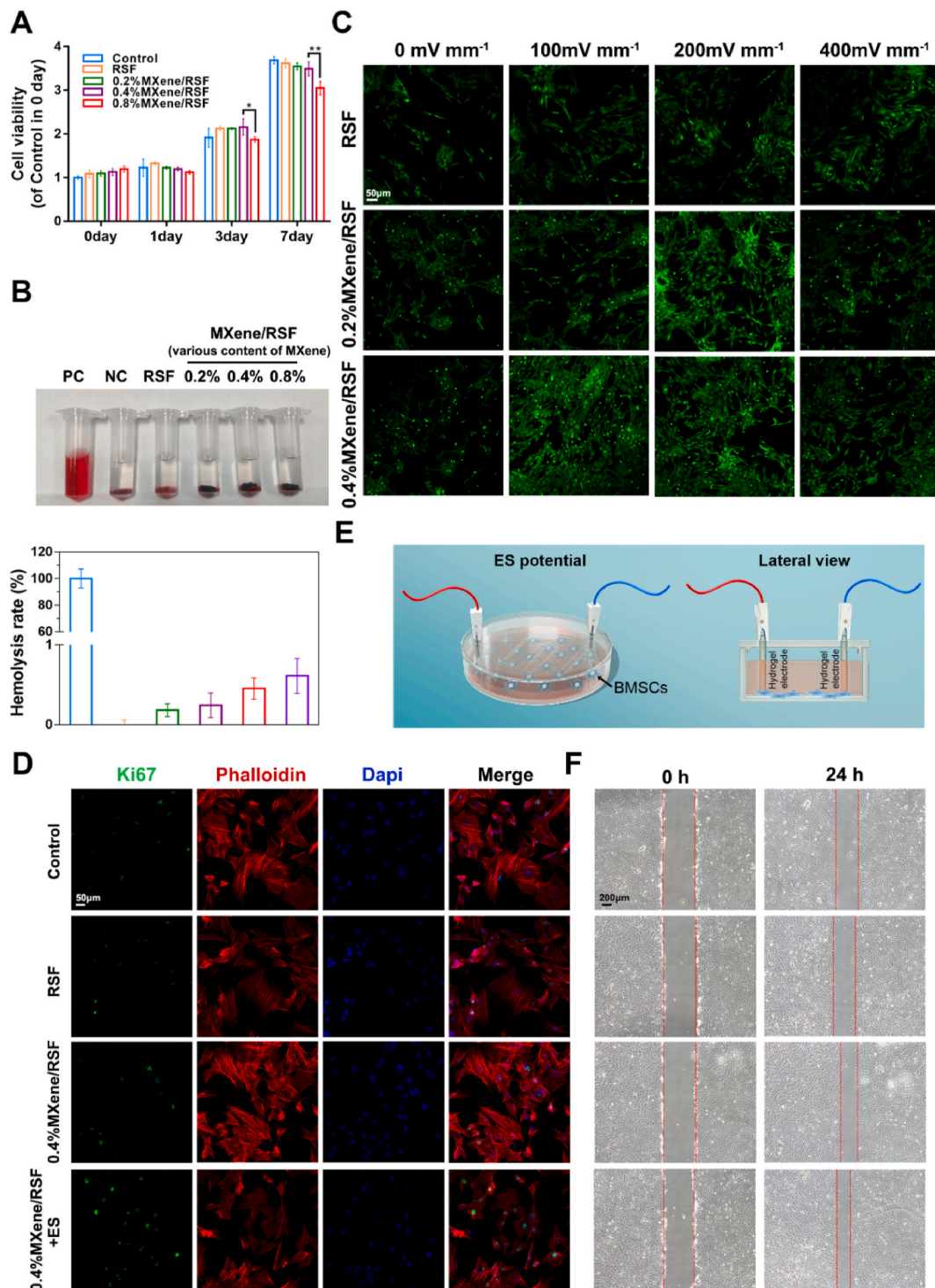
Fig. 4. Proliferation and migration evaluation of the BMSCs with different hydrogels. (A) CCK-8 assay evaluating the cytotoxic effects after 1–7 days co-incubation with different hydrogels. (B) Hemolysis test for the RSF-based hydrogels. PC, a positive control (distilled water); NC, a negative control (normal saline). (C) Living/dead staining on different hydrogels with varying ES potentials. (D) Immunofluorescence staining results of Ki67 proteins. (E) A custom-designed device to detect cell migration using hydrogel electrodes. (F) Wound scratch assay in different hydrogel samples with or without ES potential. $**P < 0.01$, $*P < 0.05$, $n = 3$.

(Fig. 5C–F). Similarly, as demonstrated in Fig. 5C, upregulation of RUNX-2 was observed in both 0.4%MXene/RSF and 0.4%MXene/RSF + ES groups in the nucleus, indicating that the main switch of osteogenic differentiation was turned on. Both MXene and external ES also exhibited increased expression levels of Col-1 in the cytoplasm, which is the main constituent of the bone extracellular matrix (Fig. 5D) [50]. The quantitative analyses of RUNX-2 and Col-1 proteins are shown in Fig. 5E,

F. Additionally, according to PCR results (Fig. 5G), RUNX-2, OCN, COL-1, and ALP were also upregulated at the mRNA levels in the 0.4% MXene/RSF and 0.4%MXene/RSF + ES groups when compared to those in control and RSF groups, especially in the 0.4%MXene/RSF + ES group at day 14, suggesting the degradation products of MXene in the medium and ES could jointly trigger an upregulation in the level of osteogenesis. All these experiments indicated that both the presence of MXene and
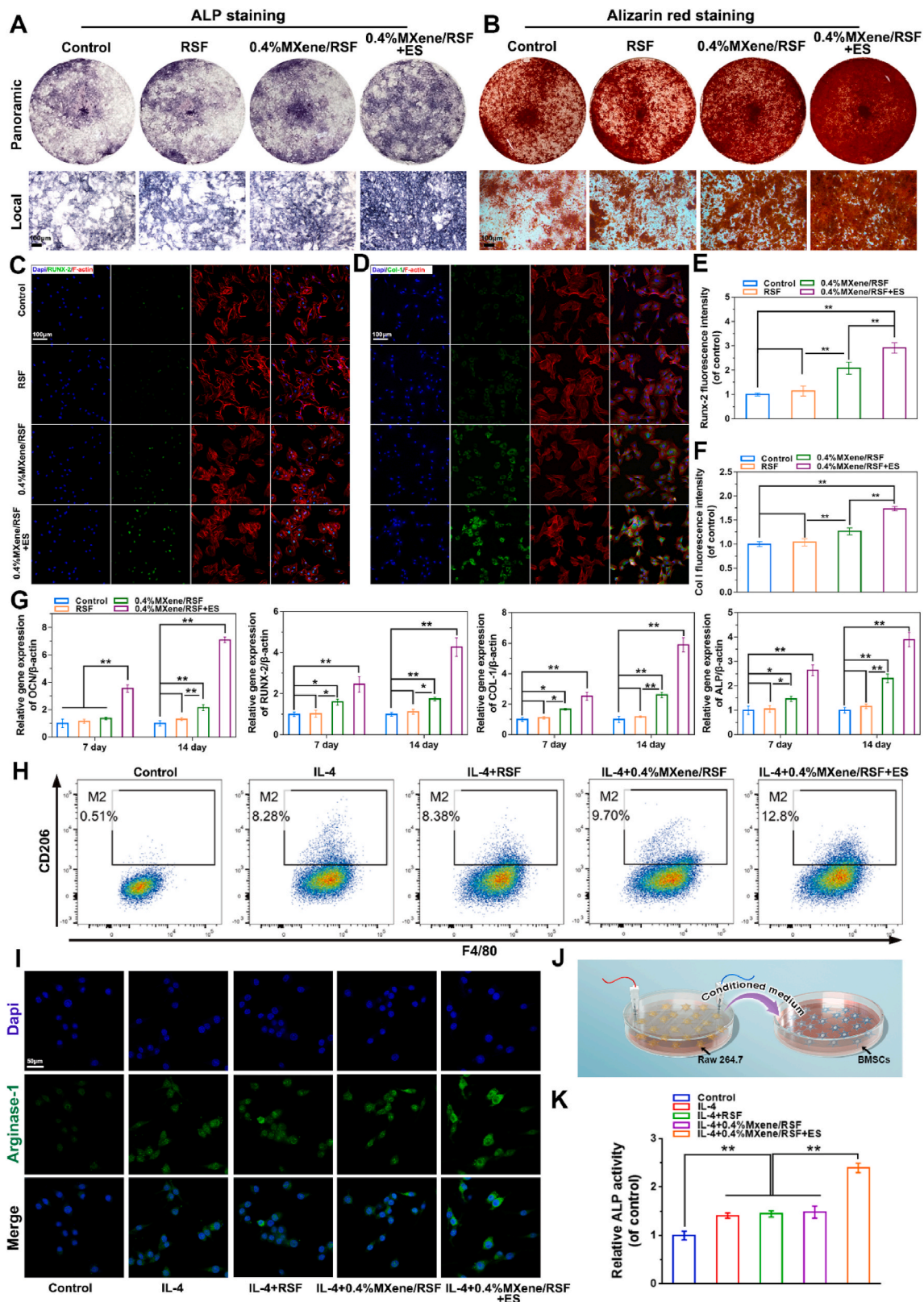
Fig. 5. Osteogenic differentiation effects of the RSF-based hydrogel samples on the BMSCs and their immunomodulatory effect on macrophage polarization in RAW264.7 cells with or without ES. (A, B) Representative photographs of ALP staining on day 7 and ARS staining on day 21. (C–F) Representative immunofluorescence staining and quantitative analysis of Runx-2 and Col-1 proteins after 7 days. (G) Real-time PCR results for the mRNA expression of OCN, Runx-2, Col-1, and ALP on day 7 and 14. (H) Flow cytometry results of the percentage of CD206$^+$F4/80$^+$cells treated with different interventions for 48 h. (I) Representative immunofluorescence staining of Arginase-1. (J) Schematic diagram showing the process of osteogenic differentiation of BMSCs regulated by macrophage M2 polarization. (K) Quantitative analysis of ALP staining of BMSCs after being cultured using the conditioned medium of RAW264.7 cells for 7 days. $**P < 0.01$, $*P < 0.05$, $n = 3$.

external ES facilitated the process of direct osteogenesis by interacting with BMSCs.

Macrophages regulate tissue regeneration and remodeling in the osteoimmune microenvironment by macrophage polarization (pro-inflammatory M1 phenotype or pro-healing M2 phenotype) [51,52]. Classical markers including arginase-1 and CD206 are widely accepted to define M2 polarization [53,54]. A flow cytometry analysis was adopted, whose results revealed that the expression levels of markers of M2 macrophages (CD206+F4/80+) was obviously increased in the IL4+0.4%MXene/RSF + ES group when compared with that in the IL4, IL4+RSF, and IL4+0.4%MXene/RSF groups (Fig. 5H). However, no statistical differences were found between IL4, IL4+RSF, and IL4+0.4% MXene/RSF groups, suggesting that it was the ES, rather than MXene, that promoted macrophage M2 polarization (Fig. S13A). In addition, similar trends were also found involving the expression of arginase-1 (Fig. 5I, and **S13B**). We also co-cultured BMSCs with macrophage-conditioned media to investigate the effect of M2 macrophages on BMSCs (Fig. 5J). We found that M2 macrophages induced by IL4+0.4%MXene/RSF + ES further enhanced the ALP staining (Fig. 5K, and **S14**), which demonstrated that M2 macrophages could regulate the osteogenic differentiation of BMSCs indirectly.

2.5. MXene/RSF hydrogels with ES stimulate neovascularization in vitro

Neovascularization plays a critical role throughout bone regeneration and skeletal development [55,56]. In general, during the process of vasculogenesis, cell viability, migration, and tube formation are usually assessed by using the human umbilical vein endothelial cells (HUVECs) [57]. In detail, the viability of HUEVCs was detected using living/dead staining and the CCK-8 assay, which showed no significant difference among the four groups (Fig. 6A, **B**). These results indicated the reasonable biocompatibility of this hydrogel system. To evaluate the migration of HUEVCs, a scratch wound healing assay was adopted. As shown in Fig. 6C, **D**, compared with the control and RSF groups, groups containing MXene, especially the 0.4%MXene/RSF + ES group, significantly enhanced the migration ability of HUEVCs. Besides, similar trends were also observed in tube formation, where more honeycomb-like structures were found in 0.4%MXene/RSF and 0.4% MXene/RSF + ES groups for 12 h (Fig. 6E). And the 0.4%MXene/RSF + ES group indicated the best angiogenic effect. The number of meshes and master junction assays were used to quantify the tube formation capacity, where more meshes and master junctions were detected in the 0.4%MXene/RSF + ES group in accordance with the results above (Fig. 6F, **G**). Altogether, these results demonstrated that both MXene and ES could synergistically enhance the process of vasculogenesis *in vitro* with good biocompatibility.

2.6. Conductive MXene/RSF hydrogels for in vivo bone-tissue engineering

For further assessing the effects of the electroactive MXene/RSF hydrogels on bone regeneration and mineralization, cranial defect models (Fig. 7A) were established by localized implantation of MXene/RSF into bone defects, according to previous studies [58,59]. At 6 and 12
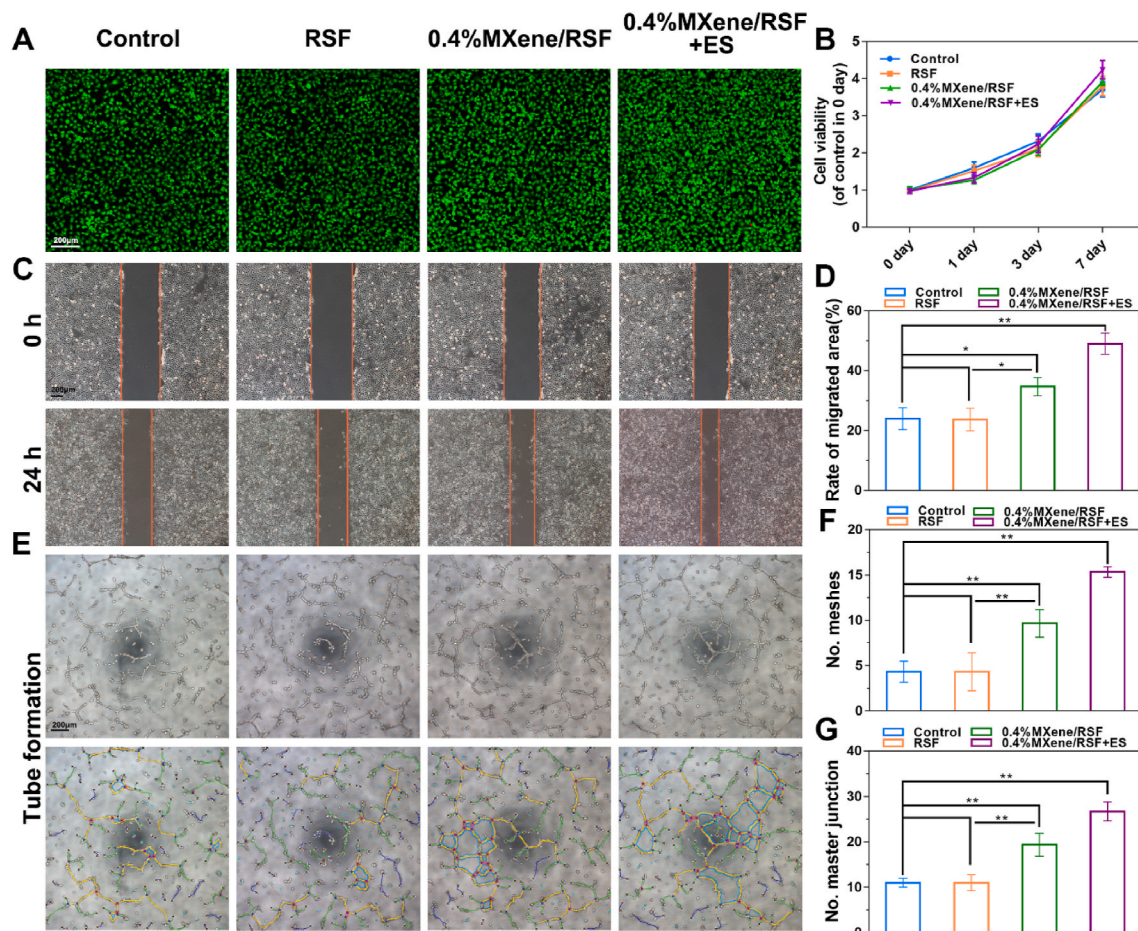
Fig. 6. Neovascularization stimulated by RSF-based hydrogels with or without ES. (A) Living/dead staining of HUVECs using different hydrogels with or without ES potential for 3 days. (B) Proliferation of HUVECs for 1, 3, and 7 days using the CCK-8 assay. (C, D) Wound scratch assay and quantitative analysis using HUVECs for 24 h. (E) Tube formation of HUVECs stimulated by RSF-based hydrogels and ES for 12 h. (F, G) Number of meshes and number of master junctions calculated using ImageJ. **$P < 0.01$, *$P < 0.05$, $n = 3$.
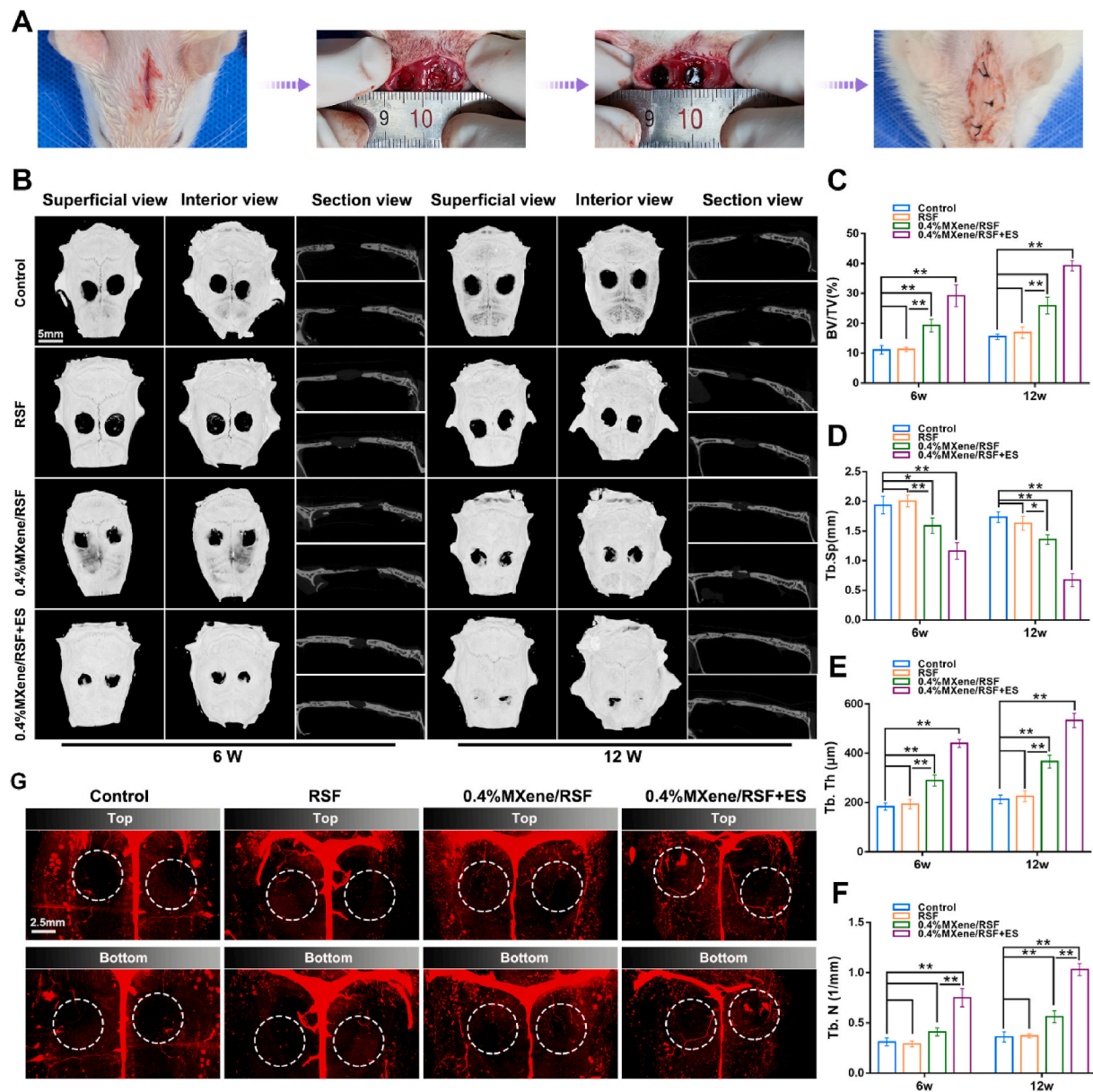
Fig. 7. MXene/RSF hydrogels with ES potential accelerated bone regeneration. (A) Procedure for the establishment of the calvarial defect model in SD rats. (B) Cranial bone regeneration at 6 and 12 weeks after implantation presented by micro-CT. (C–F) BV/TV, Tb.Sp, Tb.Th, and Tb.N results calculated based on micro-CT. (G) Representative images of 3D reconstruction of the blood vessels at 12 weeks post-implantation. $**P < 0.01$, $*P < 0.05$, $n = 3$.

weeks after implantation, micro-CT, including 3D reconstructions and 2D images, were conducted to observe new bone growth in the calvarial defects (Fig. 7B). At 6 weeks, more newly regenerated and infiltrated bone around the edge of the defects was observed in the 0.4%MXene/RSF and 0.4%MXene/RSF + ES groups, whereas no obvious new bone formation was observed in the control or pure RSF groups. Meanwhile, representative sagittal sections also showed that the 0.4% MXene/RSF group, and especially the 0.4%MXene/RSF + ES group, had more bone regeneration. At 12 weeks, the tendency for osteogenesis in the 0.4%MXene/RSF + ES group was more distinct. Based on the quantitative micro-CT analysis, bone volume fraction (BV/TV), trabecular separation (Tb.Sp), trabecular thickness (Tb.Th), and trabecular number (Tb.N) were analyzed to compare the degree of bone regeneration (Fig. 7C–F). A quantitative analysis (Fig. 7C) of the BV/TV indicated that limited bone regeneration was observed in the control and RSF groups, whereas more new bone formation was found in the 0.4% MXene/RSF and 0.4%MXene/RSF + ES groups. A similar phenomenon

was also observed for Tb.N and Tb.Th (Fig. 7E, **F**), while Tb.Sp was inhibited (Fig. 7D). Microflow perfusion and angiography combining micro-CT observation were performed to evaluate the *in vivo* vasculogenesis surrounding the hydrogels. As shown in Fig. 7G, denser vascular networks in the 0.4%MXene/RSF + ES were visually presented by 3D reconstruction of newborn vessels, suggesting an excellent angiogenic performance corresponding to the *in vitro* results. Thus, as verified by both the *in vitro* and *in vivo* results, the MXene/RSF hydrogel with external ES has the potential to become a promising strategy for bone regeneration with poor circulation.

To further confirm the osteogenic capacity of the composite hydrogel and observe the detailed morphology of the newly formed bone and expression of specific proteins, histological analyses, including toluidine blue staining, van Gieson staining, Masson staining, and fluorescent staining using undecalcified or decalcified samples, were performed (Fig. 8A–H). Corresponding to the results *in vitro*, at 12 weeks after implantation, more new bone formation in the 0.4%MXene/RSF and
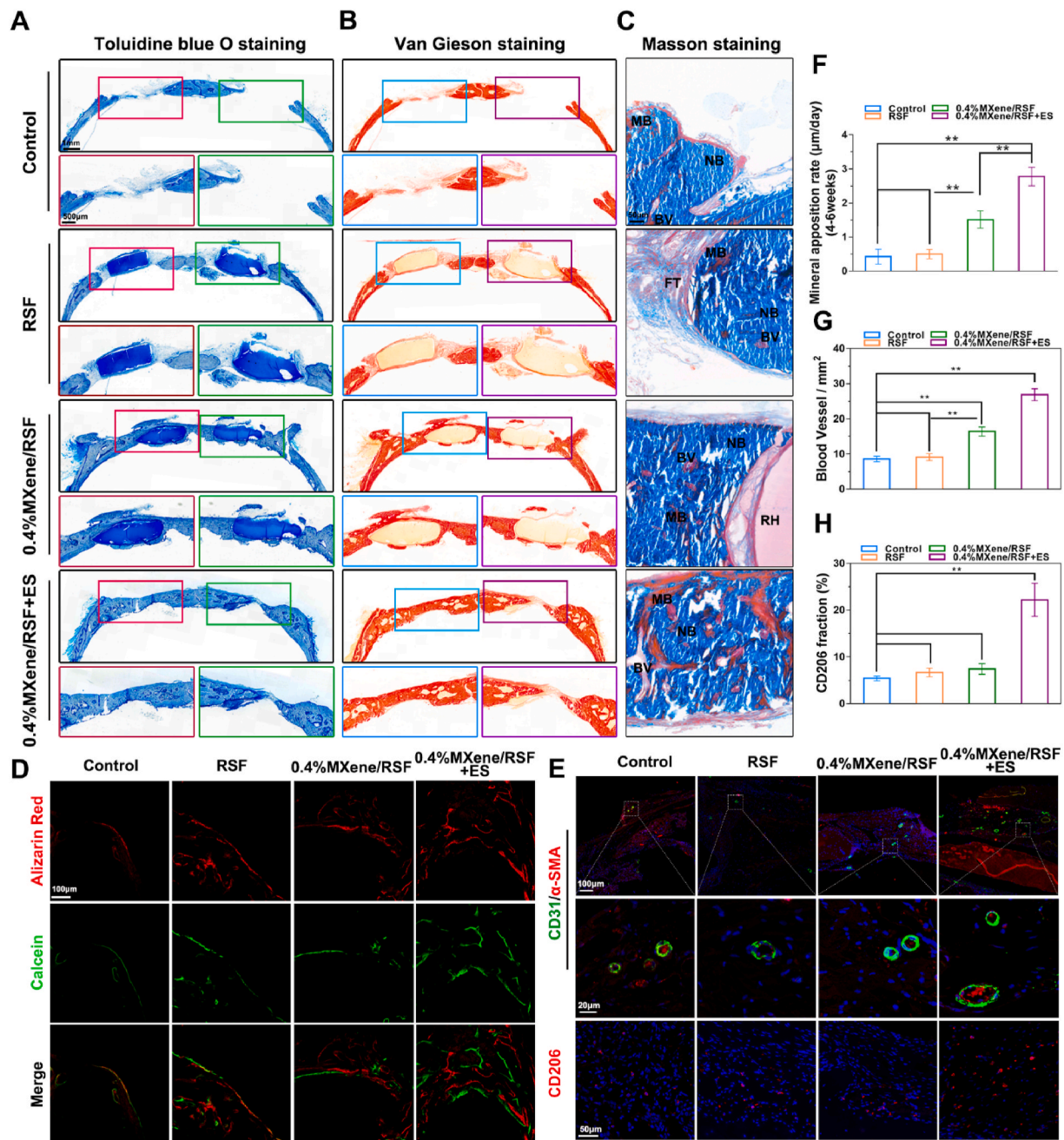
Fig. 8. Histological staining and fluorescent imaging of the calvarial defect to assess new bone formation. (A) Toluidine blue, (B) van Gieson, and (C) Masson staining of undecalcified femoral sections at 12 weeks. IB, immature bone; MB, mature bone; BV, blood vessel; FT, fibrous tissue. (D) Representative images showing calcein and alizarin red staining. (E) Immunofluorescence staining for CD31 (green) and CD206 (red) in decalcified bone tissues. Nuclei were labeled using DAPI (blue). (F) Quantitative evaluation of MAR at 4–6 weeks post-implantation. (G) Quantitative analysis of the newly formed blood vessels at 12 weeks post-implantation. (H) Quantitative analysis of the CD206 positively stained cells. $**P < 0.01$, $*P < 0.05$, $n = 3$.

0.4%MXene/RSF + ES groups was detected when compared to that in the control and blank groups according to the toluidine blue staining (Fig. 8A). Particularly, in the 0.4%MXene/RSF + ES group, almost all the bone defects on calvaria were confluent, indicating an excellent osteogenic capacity of the MXene/RSF hydrogels under ES. Van Gieson staining was also adopted to investigate the response of osteocollagenous fibers surrounding the hydrogels at 12 weeks. As shown in the magnified region of Fig. 8B, the 0.4%MXene/RSF and 0.4%MXene/RSF + ES mineralized hydrogels directly contacted with the red stained bone tissue, suggesting the degradation products of hydrogels were well integrated with the osteocollagenous fibers, while minimal fibrous capsules were observed forming in both the control and RSF groups.

Meanwhile, Masson staining results also suggested that sections from MXene containing groups (especially in 0.4%MXene/RSF + ES group) showed increased bone formation compared to the pure RSF and control groups (Fig. 8C). Moreover, far more mature bone formation (red stained) and angiogenesis was found in the 0.4%MXene/RSF + ES group, indicating its unique advantages in bone regeneration.

Alizarin red (4 weeks postoperatively) and calcein (6 weeks postoperatively) fluorescent dyes were injected intraperitoneally to explore mineral apposition rates (MAR). Alizarin red staining at 4 weeks was more pronounced in the 0.4%MXene/RSF and 0.4%MXene/RSF + ES groups (Fig. 8D), suggesting new bone formation during the earlier period of bone regeneration. MAR indicates the distance between

sequential fluorescent labels. The MAR in the groups containing MXene (especially in 0.4%MXene/RSF + ES group) showed a significant higher level than the groups without MXene or ES (Fig. 8F). These data further indicated that both MXene and ES could enhance the rate of mineralization.

Additionally, immunofluorescence for specific protein markers was performed using decalcified samples. Immunofluorescence analysis for α-SMA/CD31 revealed more newly formed blood vessels in 0.4% MXene/RSF + ES group in the cranial defect (Fig. 8E). As the quantitative results showed (Fig. 8G), the number of newly formed blood vessels increased in both the 0.4%MXene/RSF and 0.4%MXene/RSF + ES groups, and the degree of vessel formation was highest in the 0.4% MXene/RSF + ES group, implying that the MXene/RSF hydrogel could facilitate the formation of blood vessels under ES. CD206 immunofluorescence analysis was used to assess the macrophage M2 polarization *in vivo* (Fig. 8E, H). These results revealed that external ES promoted M2 macrophage infiltration to regulate the bone immune environment. To exclude the contribution of the only ES on cellular behaviors and bone regeneration, we studied its effects on the osteogenic differentiation of BMSCs *in vitro* and presented the full results *in vivo* accordingly (Fig. S15). As shown in Figs. S15A–D, ES in 0.4%MXene/RSF + ES group could induce more obvious enhancement in ALP and ARS staining than ES in RSF group, excluding the contribution of the only ES on cellular behaviors and bone regeneration. Quantitative analysis of ALP and ARS also confirmed these results. Meanwhile, more bone regeneration was observed in the 0.4%MXene/RSF + ES group than in the RSF + ES group, further suggesting that only ES could not induce the optimal bone regeneration (Fig. S15E). Similar results were also found involving the expression of CD31 and CD206, excluding the contribution of the only ES on formation of blood vessels and macrophage M2 polarization *in vivo* (Figs. S15F–H). In summary, the excellent bone repairing ability of the 0.4%MXene/RSF + ES group may be ascribed to two factors: (i) MXene is degraded to release Ti-based species since the exposure to water and oxygen, which may promote osteogenesis and neovascularization. Cui et al. demonstrated that MXene have highly efficient therapeutic effects for osteogenic differentiation by activating the WNT/HIF-1α-mediated metabolism reprogramming [60]. Meanwhile, it was also reported that Ti-molecules couple with osteogenesis and angiogenesis processes by upmodulating the PI3K/AKT signaling pathway [61]. (ii) ES regulates the electrical microenvironment to further enhance bone regeneration, modulate bone immunity, and promote angiogenesis. In addition, tissue toxicity was further evaluated using HE staining of the major organs. No obvious differences were found among the groups, suggesting high histocompatibility of the composite hydrogels (Fig. S16). Furthermore, the biodegradability and biosafety of MXene/RSF hydrogel were also evaluated *in vivo* by subcutaneous implantation. As shown in Fig. S17, the MXene/RSF hydrogel was gradually absorbed after 2 weeks of implantation. Fibroblasts began to visibly grow into the hydrogel at 4 weeks with the degradation of hydrogel and it was completely infiltrated by the surrounding tissues at 8 and 12 weeks, indicating the gradual degradation of the hydrogels *in vivo*. Meanwhile, there was no significant difference between the control and the 0.4%MXene/RSF group with respect to their levels of white blood cells (WBC), red blood cells (RBC), hemoglobin (HGB), alanine aminotransferase (ALT), aspartate aminotransferase (AST), blood urea nitrogen (BUN), and creatinine (CRE), indicating that the degradation of hydrogel products *in vivo* did not cause an evident systemic toxicity.

2.7. Underlying mechanism of osteogenic differentiation based on RNA sequencing

According to the abovementioned results, ES and the MXene/RSF hydrogels were the best combination by which to enhance bone regeneration. To explore the potential molecular mechanisms of MXene/RSF-induced osteogenic effects under ES, we performed an RNA-seq assay combining with expression profiling. After electrical stimulation of

BMSCs, we identified 1091 upregulated and 1264 downregulated differentially expressed genes (DEGs) in a volcano plot (Fig. S18). The DEGs were then subjected to functional enrichment analysis. The top 25 GO biological processes, including biomineral tissue development, biomineralization, bone mineralization, ossification, and osteoblast differentiation, were significantly enriched (Fig. 9A). Clusterprofiler was used for the GSE analysis of the sequencing results (Fig. S19). Heat maps were drawn for the abovementioned biological processes with high expression levels of osteoblast-related genes, such as RUNX-2 and COL-1, in the ES group (Fig. S20), further verifying the osteogenic effect in our current experiments.

We enriched the differentially expressed genes using the KEGG pathway and sorted them in ascending order by FDR value and found that the calcium-signaling pathway was identified in the first 25 entries, and this pathway is reportedly involved in the cell reception of electrical stimulation (Fig. 9B). Heat maps were generated for this pathway (Fig. 9C). The calmodulin (CALM) gene, which acts as a key transporter involved in Ca^{2+} transport, attracted our attention [62]. The CALM protein is a main downstream molecule of the calcium-signaling pathway, and the increase in intracellular Ca^{2+} can promote the binding of Ca^{2+} to this regulatory protein [63]. CALM gene expression was increased according to our RNA-seq analysis. To investigate whether Ca^{2+}/CALM signaling is a key target for ES treatment (Fig. 9D), we used a calcium colorimetric assay kit (Fig. 9E) and western blotting (Fig. 9F, **G**) to verify the underlying mechanism. As shown by the intracellular Ca^{2+} test in Fig. 9E, we found that ES-induced increases in intracellular Ca^{2+} could be significantly inhibited by calmidazolium, a specific antagonist of CALM. Similarly, upregulation of indicators of osteogenesis induced by ES were also inhibited by calmidazolium according to the western blotting results (Fig. 9F, **G**), suggesting that ES-induced osteogenic effects were associated with the activation of Ca^{2+}/CALM signaling. As expected (Fig. 9H, and S21), representative histochemical staining revealed that the most positive-stained cells or areas for CALM and COL-1 were observed in the MXene/RSF + ES group, further indicating that providing external ES exhibited more potentials in the enhancement of osteogenesis and may activate the Ca^{2+}/CALM signaling pathway.

3. Conclusion

In general, we have designed a novel conductive RSF hydrogel by introducing 2D bioencapsulated MXene nanosheets into an enzyme-crosslinked network for bone regeneraiton. MXene nanosheets acted as a nanostructured template to induce the selective self-assembly of RSF nanofibrils. A multifunctional hydrogel was then developed based on RSF and bioencapsulated MXene and used to systematically explore the underlying cellular mechanisms of the conductive materials under external ES in bone regeneration. Importantly, we found that this MXene-functionalized hydrogel could efficiently promote osteogenic differentiation by activating the Ca^{2+}/CALM signaling pathway in BMSCs. The conductive system was also observed to indirectly induce the differentiation of BMSCs into osteoblasts by enhancing M2 macrophage infiltration and polarization in the immune microenvironment. In addition, increased angiogenesis was also found when MXene and ES were present, offering nutrition and increasing the number of target cells to create an osteoblast–macrophage–endotheliocyte virtuous circle for bone formation. The current study revealed a promising strategy to promote bone regeneration by re-establishing the electrical microenvironment with bone microenvironment-specific materials.

4. Materials and methods

4.1. Preparation of two-dimensional (2D) Ti_3C_2 MXene nanosheets

First, 40 mL of etchant solution was prepared by mixing hydrochloric acid (HCl, Fisher Scientific), deionized H_2O, and hydrofluoric acid (HF,
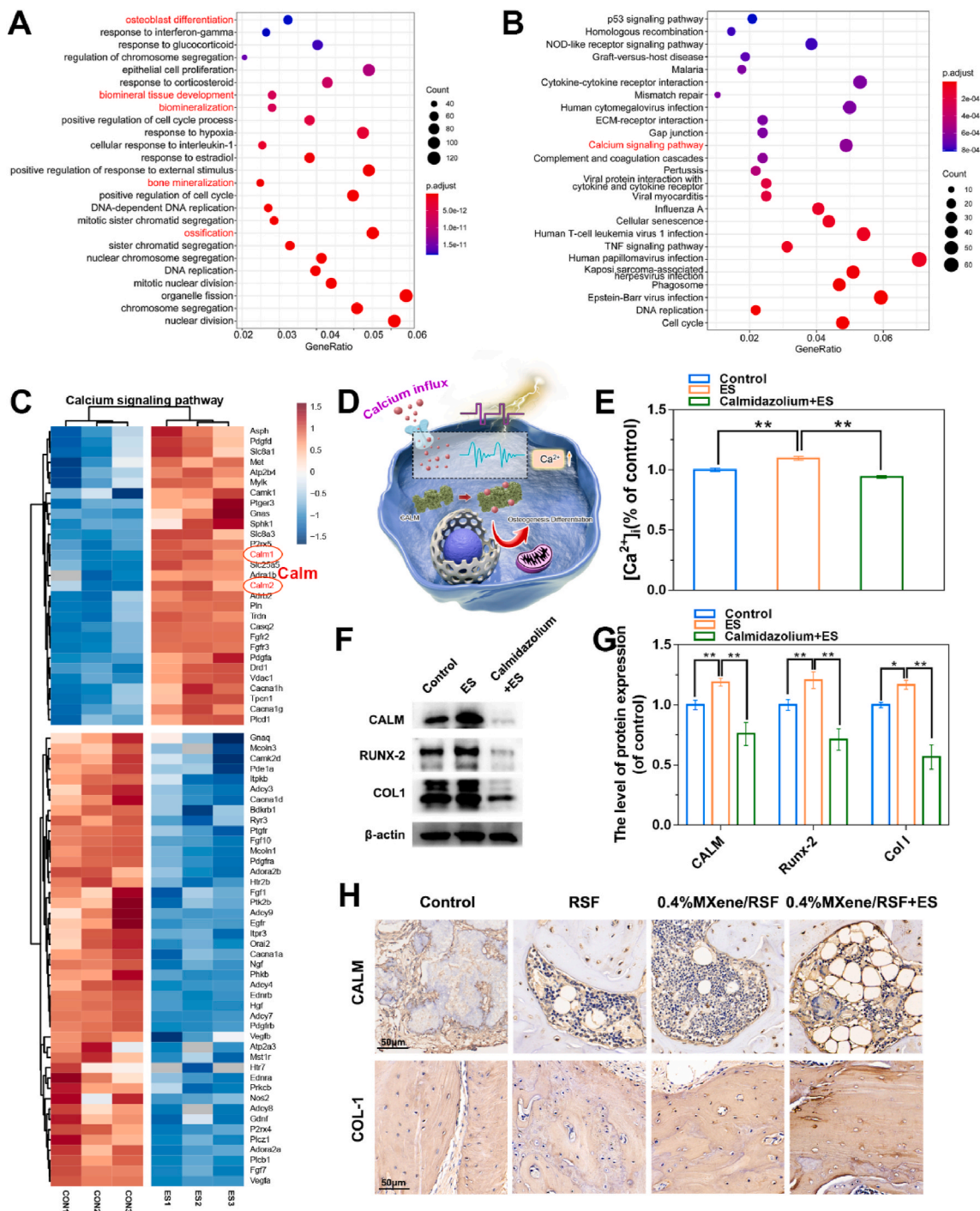
Fig. 9. Underlying molecular mechanisms of osteogenesis induced by the ES-mediated MXene/RSF hydrogel. Top 25 results from the (A) GO and (B) KEGG biological process enrichment analysis of the upregulated and downregulated DEGs. (C) Heat map summarizing the DEGs related to the calcium-signaling pathway. (D) Schematic diagram showing the potential calcium-signaling pathway. (E) Relative intracellular calcium ion concentration ($[Ca^{2+}]_i$) of BMSCs on day 7. (F, G) Protein expression levels and quantitative results of CALM, RUNX-2, and COL-1 in BMSCs with various interventions as indicated. (H) Immunohistochemical staining of CALM and COL-1 in decalcified bone tissue at 12 weeks after surgery. **$P < 0.01$, *$P < 0.05$, $n = 3$.

Sigma Aldrich) at a 6:3:1 ratio. Then, 2 g of Ti_3AlC_2 MAX phase (<38 μm) was gradually added to the etchant solution over the course of 10 min. The selective etching reaction lasted for 24 h at 35 °C under stirring. Subsequently, 150 mL of deionized H_2O was used to wash the sediment under repeated centrifugation (5 min, 3500 rpm) until the pH value of the supernatant was neutral (~6). Next, 100 mL of lithium chloride (LiCl, Sigma Aldrich) solution at the concentration of 20 g/L was mixed with the multilayer MXene sediment under stirring at 20 °C for 12 h followed by repeated centrifugation (5 min, 3500 rpm). The

supernatant was decanted until it turned dark. Another centrifugation (1 h, 3500 rpm) was adopted to decant the dilute green supernatant. Re-dispersion of the swollen sediment was achieved using deionized H_2O followed by centrifugation (10 min, 3500 rpm) to collect the single layer MXene supernatant. Then, another centrifugation (30 min, 3500 rpm) was used to optimize the flake size. The final supernatant was collected to fabricate the MXene/RSF hydrogel.

4.2. Preparation of RSF and MXene/RSF solutions and the MXene/RSF hydrogel

RSF solutions were produced according to our previously described protocol [64]. We degummed cocoons from *Bombyx mori* silkworms twice using Na$_2$CO$_3$ (0.02 M) at 100 °C for 30 min. After being rinsed thoroughly with pure water, we dried the degummed sample at 40 °C. It was then completely dissolved in LiBr (9.3 M) and simultaneously heated using a water bath (1 h, 60 °C). Dialysis was carried out against deionized water for at least 72 h at 20 °C by adopting a dialysis membrane (molecular weight cutoff = 14 kDa) to remove the residual salt. Finally, the content of RSF was evaluated using oven drying method to prepare a RSF aqueous solution (5 wt%).

A MXene/RSF solution was prepared to investigate the interactions between RSF and MXene. Briefly, MXene was added to a RSF solution at an 8:1 ratio for 30 min, followed by sonication to ensure that the nanosheets were homogeneously dispersed. Then centrifugation was conducted to remain the RSF-binding MXene. The RSF-binding MXene dispersion was placed in a 37 °C water bath for 0, 12, 36, or 72 h followed by quenching in liquid nitrogen for further experiments.

Before obtaining the MXene/RSF hydrogel, different concentrations of RSF-binding MXene (0, 2, 4, and 8 mg/mL) were added to 5 wt% RSF solutions with 20 μL/ml HRP (900 U ml^{-1}) to prepare the precursor solution. MXene/RSF hydrogel was prepared with the addition of H$_2$O$_2$ (20 μL, 0.5% v/v). All the synthetic samples should first be soaked in 75% alcohol for 12 h to strengthen their mechanical properties before obtaining the final hydrogel samples (RSF, 0.2%MXene/RSF, 0.4% MXene/RSF, and 0.8%MXene/RSF).

4.3. Materials characterization

The microstructures of both the MXene/RSF solution and MXene/RSF hydrogels were observed using SEM, cryo-SEM, and elemental mapping (Hitachi S4800, Japan). TEM images were also acquired using a JEM-2010F microscope. XRD analysis was performed using a Rigaku D/MAX-2200 PC XRD system. FT-IR spectra were acquired using a Nicolet FT-IR 6700 spectrometer. Raman scattering was recorded using a Horiba Jobin-Yvon Lab Ram HR VIS high-resolution confocal Raman microscope with an excitation laser at 785 nm. The mechanical performance of the prepared hydrogels was tested using an Instron 3367 mechanical testing instrument. The stress–strain curves and moduli of the hydrogels were also recorded accordingly. The resistance of the hydrogels with a gradient of MXene content (0, 2, 4, and 8 mg/mL) was assessed adopting a digital multimeter (Keithley DMM-6500) with a 2-wire mode and a resolution of 100 ms. Rheological experiments (37 ± 1 °C) were conducted adopting a HAAKE MARS3 thermometer (Thermo Fisher, Massachusetts, USA) with a cone-and-plate geometry of 1° incline and 60 mm diameter.

4.4. Biocompatibility evaluation of the RSF-based hydrogels

The Fudan University Animal Care and Use Committee (Shanghai, China) reviewed and approved the protocol for the animal experiments. The rat femur is a source of BMSCs, and BMSCs were cultured as described in a previous study [58]. Cell viability was tested adopting CCK-8 and living/dead cell assays, according to the manufacturer's instructions. Briefly, for the CCK-8 assay, hydrogel discs (6.9 mm diameter and 1 mm thickness) were gently placed into the 96-well plates, and BMSCs were seeded at a density of 1×10^4 cells/well. After additional incubation for 0, 1, 3, and 7 days, medium was discarded and the hydrogel discs were transferred into new 96-well plates. Next, 10% CCK-8 working solution was adopted to measure the optical density at 450 nm using a microplate reader (Leica Microsystems, Germany). Blood compatibility evaluation was performed for RSF-based hydrogels with various MXene contents (0, 2, 4, and 8 mg/mL) using hemolysis ratio testing according to a previous study [26]. Similarly, a living/dead

assay of hydrogel samples with various ES voltages (0, 100, 200, and 400 mV mm^{-1}) for 3 days was conducted using a working solution containing calcein AM (2 μM) and PI (8 μM) in 24-well plates. The pulse electrical signal (20 Hz, and 50% duty cycle) was applied for 30 min every day using JDS6600 signal generator (Junce Instrument Factory, Hangzhou, China). BMSC proliferation was evaluated using Ki67 immunofluorescence after co-culture with the hydrogel systems with or without ES for 3 days.

4.5. Scratch test

The different hydrogel systems may have different effects on BMSC migration. Thus, to improve our understanding of this, scratch tests were performed. The effects of the different hydrogel samples on cell migration *in vitro* were tested using a wound healing assay in a custom-designed device with hydrogel electrodes (Fig. 4E), which ensured the current flowed only through hydrogels, thereby confirming the influence of ES on cell migration. Meanwhile, the co-culture of hydrogel electrodes with BMSCs will sustainedly release degradation products, which can determine the influence of different hydrogels on cell migration. BMSCs were cultured in 6-well plates until they reached at least 90% confluence for the scratch tests. A sterile pipette tip was used to scratch the BMSCs monolayer after starvation for 24 h. Finally, medium containing 0.1% FBS was added to each well with different interventions. An inverted microscope was used to record the migration positions at 0 and 24 h. The migration area was calculated using ImageJ software (NIH, Bethesda, MD, USA).

4.6. Effect of hydrogels on the osteogenic differentiation of BMSCs

To induce the osteogenic differentiation of BMSCs, an osteogenesis-inducing medium (a solution containing 5 mM β-glycerophosphate, 100 μg/mL ascorbic acid, and 10 nM dexamethasone) was used. After 7 days, a BCIP/NBT solution (Beyotime, China) was used to assess ALP expression under a microscope (Zeiss LSM710, Germany). After 21 days, alizarin red staining (0.5% alizarin red working solution) was performed to evaluate the calcium deposition by. Indicators of osteogenesis, including quantitative real-time PCR analysis (RUNX-2, OCN, ALP, and COL-1) and immunofluorescence analysis (RUNX-2 and COL-1), were also studied.

4.7. RNA sequencing and mechanism validation

After 7 days of co-culture with the 0.4%MXene/RSF hydrogel plus ES, the total RNA was harvested from the BMSCs adopting TRIzol reagents. Differential expression analysis was conducted adopting the DESeq R package (2012). A q value < 0.05 and foldchange >2 and < 0.5 were set as the thresholds for significantly differential expression. Western blotting was conducted to verify the molecular mechanism with different interventions, including the control, ES, and calmidazolium plus ES groups. The conductive medium in the last two groups was MXene/RSF hydrogel. The concentration of calmidazolium was 10 μM.

4.8. Determination of intracellular Ca^{2+} concentration

The adhesive BMSCs were washed using PBS and lysed using a Calcium Colorimetric Assay Kit, according to the manufacturer's instructions (Beyotime Institute of Biotechnology, Shanghai, China). Afterward, centrifugation was conducted at 12,000 g for 3 min. The supernatant was carefully collected and added to a 96-well plate containing the detection solution, and the absorbance was measured at 575 nm after co-incubation for 5 min at 20 °C in the dark.

4.9. Evaluation of macrophage polarization

RAW264.7 cells (1×10^5 cells/well) were seeded in 6-well plates and

subjected to different interventions (Control, IL4, IL4+RSF, IL4+0.4% MXene/RSF, and IL4+0.4%MXene/RSF + ES) for 48 h. The concentration of IL4 was 20 ng/mL. The supernatants from different samples were collected to investigate the regulatory role of RAW264.7 macrophages in response to the osteogenesis of the BMSCs (supplement:supernatant = 1:1). Additional ALP staining was performed to clarify the effects of the macrophages on osteogenesis. Adherent cells were detached by scraping and collected for the flow cytometry analysis with antibodies against F4/80 and CD206, as well as immunofluorescence analysis with arginase-1.

4.10. Vasculogenesis assay

HUVECs obtained from the Cell Bank of Shanghai Institutes for Biological Sciences were used to evaluate the effects of the MXene/RSF hydrogels with or with ES on cell migration and tube formation. Endothelial cell medium (ScienCell, Carlsbad, CA, USA) was adopted for cell culture. Living/dead fluorescence staining was observed adopting calcein AM and PI for 3 days. For the migration assay, 6-well plates were used to culture HUVECs until the cell density reached at least 90% confluence. A sterile pipette tip was adopted to create a cell-free wound zone by scraping the monolayer, followed by another 12 h of various interventions (Control, RSF, 0.4%MXene/RSF, and 0.4%MXene/RSF + ES). For the tube formation assay, 24-well plates were firstly pre-treated using polymerized Matrigel and then HUVECs were seeded on top. After 12 h of intervention, representative images were recorded and parameters, including the number of meshes and master junctions, were calculated adopting ImageJ.

4.11. Construction of calvarias defect models

Surgery was performed on sixty-three Sprague-Dawley rats (300–350 g, 12 weeks) for the calvarial defect models. Briefly, to better expose the surface of calvarium, a linear skin incision was created along the median of the calvarium after anesthesia. Two bicortical channels with a diameter of 5 mm were then created using a slow-speed electric trephine drill. The bone fragments in the drilled holes were rinsed and the defects implanted with various hydrogel samples. Ultimately, the periosteum and dermis were closed using a 5-0 silk suture, followed by carprofen administration at 2 mg kg^{-1}. The 0.4%MXene/RSF hydrogel with two needle-shaped metal electrodes was used to provide an external electric field stimulation (pulse electrical signal, 20 Hz, and 50% duty cycle) at the defect site. Electrostimulation, with an electric field of 100 mV mm^{-1}, was applied for 0.5 h every other day.

4.12. Micro-computed tomography (micro-CT) analysis

Bone regeneration was assessed 6 and 12 weeks postoperatively at the defect site using a micro-CT analysis with a pixel resolution of 18 μm (SkyScan 1176, Bruker, USA). CTAn software (version 1.17.7.2) was used to quantify Tb.Th, BV/TV, Tb.SP, and Tb.N after 3D reconstruction. Representative sections were obtained from the sagittal view to observe the bone growth. After 12 weeks, 12 rats were euthanized and sequentially perfused using heparinized saline and 4% paraformaldehyde solution. When the limbs of rats become markedly stiff, cardiac perfusion with Microfl (MV-112, Flow Tech, Inc., Carver, MA) was performed. In order to better solidify the contrast medium, rats were treated at 4 °C overnight and the specimens were collected and fixed in 4% paraformaldehyde solution. After decalcification, micro-CT and CTVox software (version 3.3) were adopted to scan to the vessels surrounding the sites of bone defect.

4.13. Histological analysis

For the slicing of the undecalcified bones, calvarial bones were collected at 6 and 12 weeks postoperatively, followed by dehydration

using ethanol and polymerization in methyl methacrylate. They were then sectioned at 60 μm using a Leica Microtome (Wetzlar, Germany). Toluidine blue, van Gieson, and Masson staining were adopted to stain the sections. Sequential fluorescence labels were used to determine the mineralization rates. Alizarin red (30 mg kg^{-1}) and calcein (20 mg kg^{-1}) were injected peritoneally at 4 and 6 weeks postoperatively, respectively. In each group, three rats were sacrificed, and the mineral apposition rate (MAR) was analyzed based on the distance between the green fluorescence and red fluorescence labels at 8 weeks. For the slicing of the decalcified bone tissues, 10% EDTA solution was used to decalcify the samples. After decalcification for 6 weeks, an alcohol gradient was adopted to dehydrate the samples followed by an embedment with paraffin blocks. Continuous coronal sections (5 μm thickness) of each calvarium were collected, and stained with immunohistochemical staining (COL-1 and CALM) and immunofluorescent staining (CD31, α-SMA, and CD206). The stained sections were then digitally recorded using a microscope.

4.14. Statistical analysis

A minimum of three replicates that were independent was used for each experiment. The mean ± standard deviation (S.D.) was used to present continuous variables. One-way or two-way analysis of variance (ANOVA) followed by Tukey's test was used to compare the different treatment interventions in SPSS 20.0. Statistical significance was set at $P < 0.05$.

Data availability statement

The data that support the findings of this study are available from the corresponding author upon reasonable request.

CRediT authorship contribution statement

Zhi-Chao Hu: Conceptualization, Methodology, Investigation, Writing – original draft. **Jia-Qi Lu:** Conceptualization, Methodology, Formal analysis, Writing – original draft. **Tai-Wei Zhang:** Conceptualization, Methodology, Formal analysis, Writing – original draft. **Hai-Feng Liang:** Methodology, Formal analysis, Writing – review & editing. **Hao Yuan:** Methodology, Writing – review & editing. **Di-Han Su:** Supervision, Writing – review & editing. **Wang Ding:** Supervision, Writing – review & editing. **Rui-Xian Lian:** Formal analysis. **Yu-Xiang Ge:** Methodology, Formal analysis. **Bing Liang:** Methodology, Formal analysis. **Jian Dong:** Conceptualization, Supervision, Funding acquisition. **Xiao-Gang Zhou:** Conceptualization, Supervision, Funding acquisition. **Li-Bo Jiang:** Conceptualization, Supervision, Funding acquisition.

Declaration of competing interest

The authors declare that they have no known competing financial interests or personal relationships that could have appeared to influence the work reported in this paper.

Acknowledgements

Appendix A. Supplementary data

Supplementary data to this article can be found online at https://doi.org/10.1016/j.bioactmat.2022.08.025.

References

[1] W.A. Catterall, G. Wisedchaisri, N. Zheng, The chemical basis for electrical signaling, Nat. Chem. Biol. 13 (5) (2017) 455–463.

[2] A.H. Rajabi, M. Jaffe, T.L. Arinzeh, Piezoelectric materials for tissue regeneration: a review, Acta Biomater. 24 (2015) 12–23.

[3] G. Thrivikraman, P.S. Lee, R. Hess, V. Haenchen, B. Basu, D. Scharnweber, Interplay of substrate conductivity, cellular microenvironment, and pulsatile electrical stimulation toward osteogenesis of human mesenchymal stem cells in vitro, ACS Appl. Mater. Interfaces 7 (41) (2015) 23015–23028.

[4] B. Mollon, V. da Silva, J.W. Busse, T.A. Einhorn, M. Bhandari, Electrical stimulation for long-bone fracture-healing: a meta-analysis of randomized controlled trials, J. Bone Joint Surg. Am. 90 (11) (2008) 2322–2330.

[5] M. Eischen-Loges, K.M.C. Oliveira, M.B. Bhavsar, J.H. Barker, L. Leppik, Pretreating mesenchymal stem cells with electrical stimulation causes sustained long-lasting pro-osteogenic effects, PeerJ 6 (2018) e4959.

[6] Z. Liu, L. Dong, L. Wang, X. Wang, K. Cheng, Z. Luo, W. Weng, Mediation of cellular osteogenic differentiation through daily stimulation time based on polypyrrole planar electrodes, Sci. Rep. 7 (1) (2017) 17926.

[7] H. Xu, Q. Tang, D. Yan, G. Zheng, L. Shen, A multi-functionalized calcitriol sustainable delivery system for promoting osteoporotic bone regeneration both in vitro and in vivo, Appl. Mater. Today 22 (2021), 100906.

[8] C. Wang, M. Wang, K. Xia, J. Wang, F. Cheng, K. Shi, L. Ying, C. Yu, H. Xu, S. Xiao, C. Liang, F. Li, B. Lei, Q. Chen, A bioactive injectable self-healing anti-inflammatory hydrogel with ultralong extracellular vesicles release synergistically enhances motor functional recovery of spinal cord injury, Bioact. Mater. 6 (8) (2021) 2523–2534.

[9] X. Wu, M. Zhou, F. Jiang, S. Yin, S. Lin, G. Yang, Y. Lu, W. Zhang, X. Jiang, Marginal sealing around integral bilayer scaffolds for repairing osteochondral defects based on photocurable silk hydrogels, Bioact. Mater. 6 (11) (2021) 3976–3986.

[10] Y.Y. Lee, H.Y. Kang, S.H. Gwon, G.M. Choi, S.M. Lim, J.Y. Sun, Y.C. Joo, A strain-insensitive stretchable electronic conductor: PEDOT:PSS/acrylamide organogels, Adv. Mater. 28 (8) (2016) 1636–1643.

[11] G. Li, C. Li, G. Li, D. Yu, Z. Song, H. Wang, X. Liu, H. Liu, W. Liu, Development of conductive hydrogels for fabricating flexible strain sensors, Small 18 (5) (2022), e2101518.

[12] Q. Rong, W. Lei, M. Liu, Conductive hydrogels as smart materials for flexible electronic devices, Chemistry 24 (64) (2018) 16930–16943.

[13] K. Huang, Z. Li, J. Lin, G. Han, P. Huang, Two-dimensional transition metal carbides and nitrides (MXenes) for biomedical applications, Chem. Soc. Rev. 47 (14) (2018) 5109–5124.

[14] D. Tan, C. Jiang, N. Sun, J. Huang, Z. Zhang, Q. Zhang, J. Bu, S. Bi, Q. Guo, J. Song, Piezoelectricity in monolayer MXene for nanogenerators and piezotronics, Nano Energy 90 (2021), 106528.

[15] D. Lei, N. Liu, T. Su, Q. Zhang, L. Wang, Z. Ren, Y. Gao, Roles of MXene in pressure sensing: preparation, composite structure design, and mechanism, Adv. Mater. (2022), e2110608.

[16] Y. Zheng, Y. Jin, N. Zhang, D. Wang, Y. Yang, M. Zhang, G. Wang, W. Qu, Y. Wu, Preparation and characterization of $Ti_3C_2T_x$ MXene/PVDF cation exchange membrane for electrodialysis, Colloids Surf., A 650 (2022), 129556.

[17] Z. Hu, J. Lu, A. Hu, Y. Dou, S. Wang, D. Su, W. Ding, R. Lian, S. Lu, L. Xiao, Y.-L. Li, J. Dong, J. Zhou, X. Yang, L. Jiang, Engineering BPQDs/PLGA nanospheres-integrated wood hydrogel bionic scaffold for combinatory bone repair and osteolytic tumor therapy, Chem. Eng. J. 446 (2022), 137269.

[18] H.J. Lee, J.C. Yang, J. Choi, J. Kim, G.S. Lee, S.P. Sasikala, G.H. Lee, S.K. Park, H. M. Lee, J.Y. Sim, S. Park, S.O. Kim, Hetero-Dimensional 2D $Ti_3C_2T_x$ MXene and 1D graphene nanoribbon hybrids for machine learning-assisted pressure sensors, ACS Nano 15 (6) (2021) 10347–10356.

[19] C.J. Zhang, B. Anasori, A. Seral-Ascaso, S.H. Park, N. McEvoy, A. Shmeliov, G. S. Duesberg, J.N. Coleman, Y. Gogotsi, V. Nicolosi, Transparent, flexible, and conductive 2D titanium carbide (MXene) films with high volumetric capacitance, Adv. Mater. 29 (36) (2017).

[20] B. Anasori, M.R. Luhatskaya, Y. Gogotsi, 2D metal carbides and nitrides (MXenes) for energy storage, Nat. Rev. Mater. 2 (2) (2017), 16098.

[21] F. Han, S. Lv, Z. Li, L. Jin, B. Fan, J. Zhang, R. Zhang, X. Zhang, L. Han, J. Li, Triple-synergistic 2D material-based dual-delivery antibiotic platform, NPG Asia Mater. 12 (1) (2020) 15.

[22] S. Ling, C. Li, J. Adamcik, S. Wang, Z. Shao, X. Chen, R. Mezzenga, Directed growth of silk nanofibrils on graphene and their hybrid nanocomposites, ACS Macro Lett. 3 (2) (2014) 146–152.

[23] X. Rui, A.M. Grant, R. Ma, S. Zhang, V.V. Tsukruk, Naturally-derived biopolymer nanocomposites: interfacial design, properties and emerging applications, Mater. Sci. Eng. R Rep. 125 (2018) 1–41.

[24] M. Vural, H. Zhu, A. Pena-Francesch, J. Hung, B.D. Allen, M.C. Demirel, Self-assembly of topologically networked protein-$Ti_3C_2T_x$ MXene composites, ACS Nano 14 (6) (2020) 6956–6967.

[25] M.C. Krecker, D. Bukharina, C.B. Hatter, Y. Gogotsi, V.V. Tsukruk, Bioencapsulated MXene flakes for enhanced stability and composite precursors, Adv. Funct. Mater. 30 (43) (2020).

[26] L. Mao, S. Hu, Y. Gao, L. Wang, W. Zhao, L. Fu, H. Cheng, L. Xia, S. Xie, W. Ye, Z. Shi, G. Yang, Biodegradable and electroactive regenerated bacterial cellulose/MXene ($Ti_3C_2T_x$) composite hydrogel as wound dressing for accelerating skin wound healing under electrical stimulation, Adv. Healthcare Mater. 9 (19) (2020), e2000872.

[27] G. Ye, Z. Wen, F. Wen, X. Song, L. Wang, C. Li, Y. He, S. Prakash, X. Qiu, Mussel-inspired conductive Ti_2C-cryogel promotes functional maturation of cardiomyocytes and enhances repair of myocardial infarction, Theranostics 10 (5) (2020) 2047–2066.

[28] P. Bhattacharjee, B. Kundu, D. Naskar, H.W. Kim, T.K. Maiti, D. Bhattacharya, S. C. Kundu, Silk scaffolds in bone tissue engineering: an overview, Acta Biomater. 63 (2017) 1–17.

[29] J. Chen, W. Zhao, Silk fibroin-$Ti_3C_2T_x$ hybrid nanofiller enhance corrosion protection for waterborne epoxy coatings under deep sea environment, Chem. Eng. J. 423 (2018) (2021), 130195.

[30] C. Li, R. Mezzenga, The interplay between carbon nanomaterials and amyloid fibrils in bio-nanotechnology, Nanoscale 5 (14) (2013) 6207–6218.

[31] J. Zou, J. Wu, Y. Wang, F. Deng, J. Jiang, Y. Zhang, S. Liu, N. Li, H. Zhang, J. Yu, T. Zhai, H.N. Alshareef, Additive-mediated intercalation and surface modification of MXenes, Chem. Soc. Rev. 51 (8) (2022) 2972–2990.

[32] Z.Q. Wen, L. Hecht, L.D. Barron, Beta-sheet and associated turn signatures in vibrational Raman optical activity spectra of proteins, Protein Sci. 3 (3) (1994) 435–439.

[33] T. Lefèvre, M.E. Rousseau, M. Pézolet, Protein secondary structure and orientation in silk as revealed by Raman spectromicroscopy, Biophys. J. 92 (8) (2007) 2885–2895.

[34] A. Sarycheva, Y. Gogotsi, Raman spectroscopy analysis of the structure and surface chemistry of $Ti_3C_2T_x$ MXene, Chem. Mater. 32 (8) (2020) 3480–3488.

[35] A. Lipatov, M. Alhabeb, M.R. Lukatskaya, A. Boson, Y. Gogotsi, A. Sinitskii, Effect of synthesis on quality, electronic properties and environmental stability of individual monolayer Ti_3C_2 MXene flakes, Adv. Electron. Mater. 2 (12) (2016), 1600255.

[36] A. Kumar, M. Khandelwal, Amino acid mediated functionalization and reduction of graphene oxide – synthesis and the formation mechanism of nitrogen-doped graphene, New J. Chem. 38 (8) (2014) 3457–3467.

[37] T. Kuila, A.K. Mishra, P. Khanra, N.H. Kim, J.H. Lee, Recent advances in the efficient reduction of graphene oxide and its application as energy storage electrode materials, Nanoscale 5 (1) (2013) 52–71.

[38] B. Zuo, L. Liu, Z. Wu, Effect on properties of regenerated silk fibroin fiber coagulated with aqueous methanol/ethanol, J. Appl. Polym. Sci. 106 (1) (2007) 53–59.

[39] S. Huang, V.N. Mochalin, Understanding chemistry of two-dimensional transition metal carbides and carbonitrides (MXenes) with gas analysis, ACS Nano 14 (8) (2020) 10251–10257.

[40] H. Lin, C. Chen, X. Lu, H. Yao, Y. Chen, J. Shi, Two-dimensional titanium carbide MXenes as efficient non-noble metal electrocatalysts for oxygen reduction reaction, Sci. China Mater. 62 (5) (2019) 662–670.

[41] J. Zhang, L. Wan, Y. Gao, X. Fang, T. Lu, L. Pan, F. Xuan, Highly stretchable and self-healable MXene/polyvinyl alcohol hydrogel electrode for wearable capacitive electronic skin, Adv. Electron. Mater. 5 (7) (2019), 1900285.

[42] D. Su, M. Yao, J. Liu, Y. Zhong, X. Chen, Z. Shao, Enhancing mechanical properties of silk fibroin hydrogel through restricting the growth of β-Sheet domains, ACS Appl. Mater. Interfaces 9 (20) (2017) 17489–17498.

[43] H. Zhang, Z.G. Wang, Z.N. Zhang, J. Wu, J. Zhang, J.S. He, Regenerated-cellulose/multiwalled-carbon-nanotube composite fibers with enhanced mechanical properties prepared with the ionic liquid 1-allyl-3-methylimidazolium chloride, Adv. Mater. 19 (5) (2007) 698–704.

[44] C.D. McCaig, M. Zhao, Physiological electrical fields modify cell behaviour, Bioessays 19 (9) (1997) 819–826.

[45] L.-B. Jiang, D.-H. Su, S.-L. Ding, Q.-C. Zhang, Z.-F. Li, F.-C. Chen, W. Ding, S.-T. Zhang, J. Dong, Salt-assisted toughening of protein hydrogel with controlled degradation for bone regeneration, Adv. Funct. Mater. 29 (26) (2019), 1901314.

[46] J.P. Singhal, A.R. Ray, Synthesis of blood compatible polyamide block copolymers, Biomaterials 23 (4) (2002) 1139–1145.

[47] H. Jiang, X.B. Wang, C.Y. Li, J.S. Li, F.J. Xu, C. Mao, W.T. Yang, J. Shen, Improvement of hemocompatibility of polycaprolactone film surfaces with zwitterionic polymer brushes, Langmuir 27 (18) (2011) 11575–11581.

[48] G. Tai, M. Tai, M. Zhao, Electrically stimulated cell migration and its contribution to wound healing, Burn. Trauma. 6 (2018) 20.

[49] D.Y. Yan, J. Wang, L. Xu, S. Meng, W. Weng, Z. Xie, Z.Y. Wu, Z. Shen, B. Bai, L. Yang, Imperatorin promotes osteogenesis and suppresses osteoclast by activating AKT/GSK3 β/β-catenin pathways, J. Cell Mol. Med. 24 (3) (2020) 2330–2341.

[50] Y. Chen, S. Yang, S. Lovisa, C.G. Ambrose, K.M. McAndrews, H. Sugimoto, R. Kalluri, Type-I collagen produced by distinct fibroblast lineages reveals specific function during embryogenesis and osteogenesis imperfecta, Nat. Commun. 12 (1) (2021) 7199.

[51] L.-B. Jiang, S.-L. Ding, W. Ding, D.-H. Su, F.-X. Zhang, T.-W. Zhang, X.-F. Yin, L. Xiao, Y.-L. Li, F.-L. Yuan, J. Dong, Injectable sericin based nanocomposite hydrogel for multi-modal imaging-guided immunomodulatory bone regeneration, Chem. Eng. J. 418 (2021), 129323.

[52] X. Dai, B.C. Heng, Y. Bai, F. You, X. Sun, Y. Li, Z. Tang, M. Xu, X. Zhang, X. Deng, Restoration of electrical microenvironment enhances bone regeneration under

diabetic conditions by modulating macrophage polarization, Bioact. Mater. 6 (7) (2021) 2029–2038.

[53] S. Yan, M. Zhou, X. Zheng, Y. Xing, J. Dong, M. Yan, R. Li, Anti-inflammatory effect of curcumin on the mouse model of myocardial infarction through regulating macrophage polarization, Mediat. Inflamm. 2021 (2021), 9976912.

[54] S. Zhang, H. Zhang, Z. Jin, S. Wang, Y. Wang, L. Zhu, W. Sun, B. Yan, Fucoidan inhibits tooth movement by promoting restorative macrophage polarization through the STAT3 pathway, J. Cell. Physiol. 235 (9) (2020) 5938–5950.

[55] A. Marrella, T.Y. Lee, D.H. Lee, S. Karuthedom, D. Syla, A. Chawla, A. Khademhosseini, H.L. Jang, Engineering vascularized and innervated bone biomaterials for improved skeletal tissue regeneration, Mater, Today Off. 21 (4) (2018) 362–376.

[56] J. Yin, S. Pan, X. Guo, Y. Gao, D. Zhu, Q. Yang, J. Gao, C. Zhang, Y. Chen, Nb$_2$C MXene-functionalized scaffolds enables osteosarcoma phototherapy and angiogenesis/osteogenesis of bone defects, Nano-Micro Lett. 13 (1) (2021) 30.

[57] H.J. Park, Y. Zhang, S.P. Georgescu, K.L. Johnson, D. Kong, J.B. Galper, Human umbilical vein endothelial cells and human dermal microvascular endothelial cells offer new insights into the relationship between lipid metabolism and angiogenesis, Stem Cell Rev. 2 (2) (2006) 93–102.

[58] B. Yang, J. Yin, Y. Chen, S. Pan, H. Yao, Y. Gao, J. Shi, 2D-black-phosphorus-reinforced 3D-printed scaffolds: a stepwise countermeasure for osteosarcoma, Adv. Mater. 30 (10) (2018).

[59] Q. Yang, H. Yin, T. Xu, D. Zhu, J. Yin, Y. Chen, X. Yu, J. Gao, C. Zhang, Y. Chen, Y. Gao, Engineering 2D mesoporous silica@MXene-integrated 3D-printing scaffolds for combinatory osteosarcoma therapy and NO-augmented bone regeneration, Small 16 (14) (2020), e1906814.

[60] D. Cui, N. Kong, L. Ding, Y. Guo, W. Yang, F. Yan, Ultrathin 2D titanium carbide MXene (Ti$_3$C$_2$T$_x$) nanoflakes activate WNT/HIF-1α-mediated metabolism reprogramming for periodontal regeneration, Adv. Healthcare Mater. 10 (22) (2021), e2101215.

[61] B.R. Martins, T.S. Pinto, C.J. da Costa Fernandes, F. Bezerra, W.F. Zambuzzi, PI3K/AKT signaling drives titanium-induced angiogenic stimulus, J. Mater. Sci. Mater. Med. 32 (1) (2021) 18.

[62] P. Chen, Q. Wu, J. Feng, L. Yan, Y. Sun, S. Liu, Y. Xiang, M. Zhang, T. Pan, X. Chen, T. Duan, L. Zhai, B. Zhai, W. Wang, R. Zhang, B. Chen, X. Han, Y. Li, L. Chen, Y. Liu, X. Huang, T. Jin, W. Zhang, H. Luo, X. Chen, Y. Li, Q. Li, G. Li, Q. Zhang, L. Zhuo, Z. Yang, H. Tang, T. Xie, X. Ouyang, X. Sui, Erianin, a novel dibenzyl compound in Dendrobium extract, inhibits lung cancer cell growth and migration via calcium/calmodulin-dependent ferroptosis, Signal Transduct. Targeted Ther. 5 (1) (2020) 51.

[63] R.D. Zühlke, G.S. Pitt, K. Deisseroth, R.W. Tsien, H. Reuter, Calmodulin supports both inactivation and facilitation of L-type calcium channels, Nature 399 (6732) (1999) 159–162.

[64] D. Su, L. Jiang, X. Chen, J. Dong, Z. Shao, Enhancing the gelation and bioactivity of injectable silk fibroin hydrogel with laponite nanoplatelets, ACS Appl. Mater. Interfaces 8 (15) (2016) 9619–9628.